

Strongly Magnetized Tidal Disruption Event Disks via Stream Injection in GRMHD

Brandon Curd,^{1,2,3*} Richard Anantua^{1,2,3}, Hayley West¹, and Joaquin Duran¹

¹ Department of Physics & Astronomy, The University of Texas at San Antonio, One UTSA Circle, San Antonio, TX 78249, USA

² Black Hole Initiative at Harvard University, 20 Garden Street, Cambridge, MA 02138, USA

³ Center for Astrophysics | Harvard & Smithsonian, 60 Garden Street, Cambridge, MA 02138, USA

Accepted XXX. Received YYY; in original form ZZZ

ABSTRACT

Magnetically arrested accretion disks (MADs) around a rapidly rotating black hole (BH) have been proposed as a model for jetted tidal disruption events (TDEs). However, the dynamics of strongly magnetized disks in a more realistic simulation which can mimic the chaotic dynamics during a TDE have previously been unexplored. Here we employ global GRMHD simulations of a pre-existing MAD disk interacting with an injected TDE stream with impact parameter $\beta \equiv R_t/R_p = 4 - 7$ to investigate how strongly magnetized TDEs differ from the standard MAD picture. We demonstrate for the first time that a MAD or semi-MAD state can be sustained and jets powered by the BH spin are produced in a TDE. We also demonstrate that the strength of the self-intersection shock depends on how dense the disk is relative to the stream, or the density contrast $f_\rho = \rho_d/\rho_s$. The jet or funnel can become significantly tilted (by $10 - 30^\circ$) due to the self-intersection outflow when $f_\rho \leq 0.1$. In models with a powerful jet and $f_\rho \leq 0.01$, the tilted jet interacts with and ultimately tilts the disk by as much as 23 degrees from the incoming stream. We illustrate that as f_ρ increases, the tilt of the jet and disk is expected to realign with the BH spin once $f_\rho \geq 0.1$. We illustrate how the tilt can rapidly realign if f_ρ increases rapidly and apply this to TDEs which have shown X-ray evolution on timescales of days-weeks.

Key words: accretion, accretion discs - black hole physics - MHD - gamma-rays: galaxies - X-rays: galaxies

1 INTRODUCTION

When a star wanders too close to its central black hole (BH), the tidal forces from the BH exceed the self gravity of the star and the star is subsequently disrupted into a stream of stellar material (Hills 1975; Rees 1988; Phinney 1989; Evans & Kochanek 1989). The bound portion of the stream ultimately returns to the BH, delivering mass to the pericenter radius at the fall back rate (\dot{M}_{fb}) which falls off as $(t/t_{\text{fb}})^{-5/3}$, where t_{fb} is the orbital period of the most bound portion of the stream (or the fall back time). This leads to emission which also drops off as $(t/t_{\text{fb}})^{-5/3}$ since the energy available for dissipation is provided by the kinetic energy of the stream. The transient, which is known as a tidal disruption event (TDE), is typically detectable for months-years.

The dynamics governing the properties of the stream and subsequent emission depend on the stellar mass, eccentricity, pericenter radius, and compressibility of the star. The tidal radius of the star is given by,

$$R_t/r_g = 47m_6^{-2/3}m_*^{-1/3}r_*, \quad (1)$$

where $m_6 = M_{\text{BH}}/10^6 M_\odot$ is the mass of the SMBH, $m_* = M_*/M_\odot$ is the mass of the disrupted star, and $r_* = R_*/R_\odot$

is its radius. For the typical TDE, the orbit is parabolic ($e = 1$). For zero age main sequence stars the radius for complete disruption depends on the compressibility and occurs at $\sim 0.9R_t$ for $\gamma = 5/3$ and at $\gtrsim 2R_t$ for $\gamma = 4/3$ (Guillochon & Ramirez-Ruiz 2013; Mainetti et al. 2017), though it is larger for evolved stars (Golightly et al. 2019). Several works have addressed the initial disruption of the star and evolution of the stream over a broad parameter space (Carter & Luminet 1982; Evans & Kochanek 1989; Kochanek 1994; Lodato et al. 2009; Brassart & Luminet 2010; Stone et al. 2013; Coughlin & Nixon 2015; Coughlin et al. 2016; Steinberg et al. 2019; Ryu et al. 2020).

TDEs have been discovered in the X-ray, optical/UV, and radio (see Komossa 2015; Alexander et al. 2020; Gezari 2021 for a review). While disk formation is expected in TDEs, what powers the emission is still unclear, for instance either turbulent accretion or shocks could explain the emission at different stages in the evolution. The presence of outflows, possibly launched by an accretion disk (Strubbe & Quataert 2009; Coughlin & Begelman 2014; Metzger & Stone 2016), has been inferred in many cases due to radio emission (Alexander et al. 2016, 2017) and TDEs have also been observed to launch jets (Bloom et al. 2011; Burrows et al. 2011; Zauderer et al. 2011; Cenko et al. 2012; Brown et al. 2015). More recently, a handful of TDEs have been observed during the rise

* E-mail: brandon.curd@utsa.edu

to peak (Holoien et al. 2019, 2020; Hinkle et al. 2021; Hammerstein et al. 2023). This bounty of observations is expected to grow significantly once the Large Synoptic Survey Telescope (LSST, Ivezić et al. 2019; Bricman & Gomboc 2020) comes online, but theory has yet to fully describe the range of observational properties exhibited by TDEs.

Jetted TDEs have observational properties that present a particularly complicated puzzle. For instance, *Swift* J1644+57 showed rapid viability following the turn on with quasi-periodic oscillations (QPOs) at ~ 200 s (Reis et al. 2012), long period viability at $\sim 10^6$ s with the period increasing over the course of the transient (Saxton et al. 2012), and a rapid drop in the X-ray flux at the ~ 500 days after the initial trigger (Zauderer et al. 2013). A similar drop off in the X-ray flux was seen in *Swift* J2058+05 after several months (Pasham et al. 2015).

Magnetically arrested accretion disks (MADs, Narayan et al. 2003) are thought to provide a physical explanation for both the presence of a relativistic jets and variability in jetted TDEs. The large magnetic flux required for a MAD is thought to be sourced by either poloidal field lines in a fossil disk (Kelley et al. 2014; Tchekhovskoy et al. 2014; Teboul & Metzger 2023) or conversion of toroidal field lines to poloidal through a dynamo effect (Liska et al. 2020). However, general relativistic radiation magnetohydrodynamics (GRRMHD) simulations of thin MADs have not shown complete jet turn off, potentially due to magnetic pressure support of the disk at low accretion rates (Avara et al. 2016; Curd & Narayan 2023; Liska et al. 2022). Thus, the rapid shut off in X-ray flux is difficult to explain in a MAD state unless simulations are unable to capture magnetic diffusion due to their relatively short duration (typically several days).

Disk formation in TDEs may result in a different disk structure than the standard advection dominated accretion disk (ADAF, Abramowicz et al. 1988; Narayan & Yi 1995), which has been assumed in some studies (Dai et al. 2018; Curd & Narayan 2019). Several numerical studies of disk formation have demonstrated the presence of shocks and outflows as well as long lasting asymmetric structure (Ramirez-Ruiz & Rosswog 2009; Guillochon & Ramirez-Ruiz 2013; Shiohara et al. 2015; Bonnerot et al. 2016; Sadowski et al. 2016; Hayasaki et al. 2016; Bonnerot & Lu 2020; Bonnerot et al. 2021; Curd 2021; Andalman et al. 2022; Steinberg & Stone 2022; Ryu et al. 2023). Furthermore, the eccentricity of material sourced from the stream is difficult to dissipate which, in the majority of studies, leads to an eccentric accretion disk and spiral shocks. For instance, the most realistic smooth particle hydrodynamics simulations to date found imperfect circularization as the final disk remains mildly eccentric with $e \approx 0.3$ (Bonnerot & Lu 2020; Bonnerot et al. 2021). A long duration simulation ($2t_{\text{fb}}$) by Ryu et al. (2023) demonstrated that shocks may dominate the energy budget of the TDE and the disk may remain highly eccentric with $e \sim 0.5 - 0.6$. However, recent RHD simulations with adaptive mesh refinement find that the inner disk was able to reach $e < 0.2$ after more than 30 days (Steinberg & Stone 2022), which is substantially longer than disk formation simulations with similar parameters. It is worth noting that GRMHD and GRRMHD simulations were unable to reach the magnetic flux that is required for the MAD state due to the weak magnetic flux provided by the stream as well as the chaotic disk formation (Sadowski et al. 2016; Curd 2021). As there are no current simulations of

eccentric MADs nor TDE disk formation simulations which result in a MAD, it is unclear how MADs in TDEs may differ from the standard thick accretion disk.

The primary question we address in this work is whether or not TDE disks can maintain the magnetic flux required for the MAD state. Although Kelley et al. (2014) demonstrated that the stream can trap some magnetic flux, how much magnetic field threaded the BH can not be seen in their local simulations. Global simulations are needed in order to observe field lines advecting onto the BH horizon. Furthermore, the self intersection outflow is quasi spherical thus the force that it applies to the inner disk and jet is not symmetrical (e.g. Jiang et al. 2016). This suggests that the jet, during strong self intersection, will experience an asymmetric lateral force about the jet axis. One might expect strong perturbation of the jet, and potentially the disk due its interaction with the jet.

In this work, we investigate MAD or strongly magnetized TDE disks in GRMHD using a novel approach to overcome the computational difficulties in simulating the large and small scale structures, as well as long time scales, required to study TDE disks in a global simulation. We assume a BH mass of $10^6 M_{\odot}$ and stellar mass of $1 M_{\odot}$ in each simulation. We also study the effects of spin and use $a_* = 0$ and $a_* = 0.9$. We skip the initial disk formation process and assume it resulted in the existence of a circularized, small scale MAD disk, which we use as the initial conditions for each simulation. We then inject a magnetized stream with a fall back rate appropriate for a given time in the TDE evolution. We set the pericenter radius of the stream such that the self intersection radius is on the order of $50r_g$, where r_g is the gravitational radius (defined in Section 4). Since GRMHD simulations are scale free, the most important parameter in our simulations is the ratio between the density of the pre-existing disk and injected stream (or the density contrast, which we define in Section 2). We evolve each simulation for $\sim 0.87 - 4$ days and study the disk and jet properties during the interaction between the disk and stream.

This paper is organized as follows. In Section 2, we discuss how the density contrast evolves in a simplified model of the TDE stream and accretion disk and illustrate potential consequences on the dynamics. In Section 3, we describe the numerical methods used to perform the GRMHD simulations. In Section 4, we define calculations used to analyze the simulations. In Section 5, we discuss core results and provide visualizations of each simulation. We discuss how our results can describe jetted TDEs in Section 6 and we conclude in Section 7.

2 DENSITY CONTRAST IN TDES

Following Stone et al. (2013), we define the fallback time as

$$t_{\text{fb}} = 3.5 \times 10^6 \text{sec} m_6^{1/2} m_*^{-1} r_*^{3/2}. \quad (2)$$

Following the rise to peak, the mass fallback rate follows a power law

$$\dot{M}_{\text{fb}} \sim \dot{M}_{\text{peak}} \left(\frac{t}{t_{\text{fb}}} \right)^{-5/3}, \quad (3)$$

where

$$\frac{\dot{M}_{\text{peak}}}{\dot{M}_{\text{Edd}}} \sim 133 m_6^{-3/2} m_*^2 r_*^{-3/2} \quad (4)$$

is the peak mass fallback rate in units of the Eddington mass accretion rate (defined later in Equation 16). Note we set $\eta = 0.1$, $k = 1$, and $n = 0$ in each of the expressions for simplicity such that there is no dependence on β .

The simulations presented in this work demonstrate that the density contrast

$$f_\rho(t, r) = \frac{\rho_d(t, r)}{\rho_s(t, r)}, \quad (5)$$

leads to different dynamics in a TDE, where ρ_d is the mass density of the pre-existing disk and ρ_s that of the injected stream. Namely, the self-intersection outflow can be diminished if the stream's orbit is changed during its interaction with the disk. At the start of the TDE evolution, $f_\rho < 1$. Even in the simulation presented by Steinberg & Stone (2022), the circularized disk clearly remains less dense than the stream by roughly an order of magnitude. Depending on how the disk mass, scale, and geometry evolves, the quantity f_ρ could conceivably exceed unity at late times. Here we discuss how evolution of f_ρ could be relevant in TDEs.

To describe the stream, we assume that its density is related to the fallback rate by the expression

$$\rho_s(t, r) = \frac{\dot{M}_{\text{fb}}(t)}{\pi H_s(r)^2 v_s(r)}, \quad (6)$$

where H_s is the stream height and $v_s \approx \sqrt{2GM_{\text{BH}}/r}$ is the free-fall velocity, which is roughly the speed of the incoming stream. For simplicity, we assume the stream height takes the form $H_s = (r/R_p) R_* / R_p$.

To approximate the evolution of the disk, we assume that $t \geq t_{\text{fb}}$ such that the initial disk mass is $M_d(t = t_{\text{fb}}) = 0.1 M_*$. We then approximate the disk mass by accounting for mass accreted by the BH over time

$$\dot{M}_d(t) = \dot{M}_{\text{fb}}(t) - \dot{M}_{\text{BH}}(t). \quad (7)$$

Here we assume $\dot{M}_{\text{BH}} = f_{\text{acc}} \dot{M}_{\text{fb}}$, and use a fiducial value of $f_{\text{acc}} = 0.1$. This assumption is motivated by Curd (2021), which found a mass accretion rate of $\sim 10\%$ of the fallback rate. This assumption may not hold for long term evolution as the disk mass builds up (e.g. Metzger 2022). The disk mass then evolves as

$$M_d(t) = M_{d,0} + (1 - f_{\text{acc}}) \int_{t_{\text{fb}}}^t \dot{M}_{\text{fb}}(t) dt \quad (8)$$

We assume that the gas density follows a power-law with radius of $\rho_d(r, t) = \rho_{d,0}(t)(r/r_H)^{-1}$, where r_H is the horizon radius and $\rho_{d,0}(t)$ is the maximum density of the disk at time t . This profile is appropriate for a MAD disk (Chatterjee & Narayan 2022), but is also similar to that of the TDE disk in Andalman et al. (2022). The density for a disk of outer radius R_d is obtained by

$$\rho_d(t, r) = \frac{M_d(t)}{2\pi r(R_d^2 - r_H^2)} \quad (9)$$

Here we assume a spherical distribution at all mass accretion rates. At low accretion rates, the disk may collapse into a disk geometry with scale-height h_d which may have radial dependence. We set $\rho_d(r) = 0$ for $r < r_H$ and $r > R_d$.

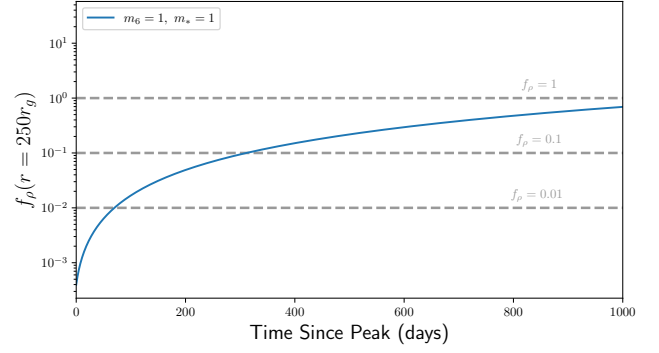


Figure 1. Here we illustrate how f_ρ evolves in our simple TDE disk model with a BH mass $m_6 = 1$ and stellar mass $m_* = 1$. Note that we set $f_{\text{acc}} = 0.1$ and $\beta = 1$ for simplicity. We show the initial f_ρ for each a_* = 0.9 simulation in Table 1 based on \dot{M}_{inj} (horizontal dashed lines). As f_ρ increases, the stream will dissipate more of its orbital energy in its interaction with the disk. As we describe in Section 5, the self intersection shock weakens as a result.

Although we have performed simulations in which the accretion disk is geometrically thick, in part because we cannot sufficiently resolve small scale-height disks, our simulations do demonstrate the impact that the density contrast has on the stream dynamics. We believe that this effect should be similar in a thin system. Furthermore, the incoming stream is expected to be aligned with the disk since the disk tends to remain roughly aligned with the initial angular momentum of the star and does not precess (Andalman et al. 2022).

We show an example of f_ρ over time using our assumed disk and stream evolution in Figure 1. In a scenario where a circularized accretion disk forms, there is not a cleared path for the stream to flow along towards pericenter. Instead, the circularized disk will exert ram pressure on the stream with an acceleration $a_{\text{ram}} \propto f_\rho$, effectively braking it. At low f_ρ , the stream will be effectively unperturbed. However, as f_ρ approaches unity, the ram pressure may completely prevent the stream from reaching pericenter. Instead, the stream may mix with the disk as it rapidly dissipates orbital energy similar to Steinberg & Stone (2022). As we show in this work, the self intersection becomes weaker as f_ρ increases, which leads to dynamic changes in the disk and jet/corona. Such evolution could be responsible for state transitions and delayed outflows, which have occurred in several TDEs. Here we have ignored the possibility of disk collapse, but we discuss how this may change TDE evolution in the context of f_ρ in Section 6.

We note that the evolution and size of the disk is a vital component of our asserted scenario. For instance, we have neglected the possibility of an extended envelope existing beyond R_{circ} as in Metzger (2022). In addition, we assume that \dot{M}_{BH} is proportional to \dot{M}_{fb} at all times. While this is based on simulation results, global simulations have yet to cover the full range of TDE evolution. In models such as Metzger (2022), bound material within the disk will also drain into the BH after an accretion time. See Metzger (2022) for a description.

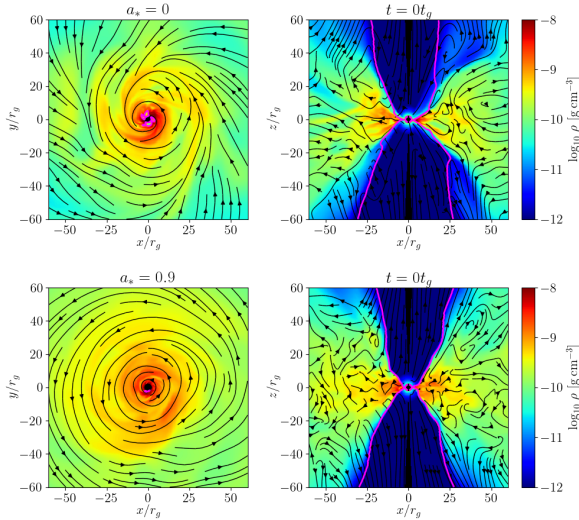


Figure 2. Initial simulation state for each BH spin. We show the gas density (colors), velocity (streamlines), and jet boundary ($\sigma = 1$, pink line).

3 NUMERICAL METHODS

We present a suite of 3D numerical simulations of MAD TDE disks carried out with the GRMHD code, KORAL (Sądowski et al. 2013, 2014, 2015; Sądowski & Narayan 2015). Using a mesh-based, finite-difference method in a stationary Kerr space-time, KORAL solves the conservation equations of GRMHD:

$$(\rho u^\mu)_{;\mu} = 0, \quad (10)$$

$$(T^\mu{}_\nu)_{;\mu} = 0, \quad (11)$$

where ρ is the gas density in the comoving fluid frame, u^μ are the components of the gas four-velocity as measured in the ‘lab frame’, $T^\mu{}_\nu$ is the MHD stress-energy tensor in the ‘lab frame’:

$$T^\mu{}_\nu = (\rho + u_g + p_g + b^2)u^\mu u_\nu + (p_g + \frac{1}{2}b^2)\delta^\mu{}_\nu - b^\mu b_\nu. \quad (12)$$

Here u_g and $p_g = (\gamma_g - 1)u_g$ are the internal energy and pressure of the gas in the comoving frame, and b^μ is the magnetic field four-vector which is evolved following the ideal MHD induction equation (Gammie et al. 2003). We adopt $\gamma = 5/3$ in this work. The code can handle radiation as well, but we choose to study pure GRMHD in this work to lower computational costs.

We evolve the fluid in modified Kerr-Schild coordinates with the inner radius of the simulation domain inside of the BH horizon. The radial grid cells are spaced logarithmically, and we choose inner and outer radial bounds $R_{\min} < r_H$ (with 4 cells within the horizon) and $R_{\max} = 5 \times 10^4 r_g$. We also use a full 2π in azimuth and set $\varphi_{\min} = -\pi$ and $\varphi_{\max} = \pi$. We choose outflow boundary conditions at both the inner and outer radial bounds, reflective boundary conditions at the top and bottom polar boundaries, and periodic boundary conditions in φ . In each simulation, we employ a resolution $N_r \times N_\vartheta \times N_\varphi = 256 \times 144 \times 144$. Specifics of the grid are given in Appendix A.

In order to study a strongly magnetized disk which resembles a TDE disk, we first initialize and evolve a MAD disk

before introducing the TDE stream. Similar to the fossil disk scenario proposed by Tchekhovskoy et al. (2014) and Kelley et al. (2014), this setup relies on the pre-existing disk to obtain the poloidal field required by a MAD. Our setup differs in that we skip the rise to peak and the interaction between the stream and fossil disk. Instead, we assume that the TDE has already obtained magnetic flux from the fossil disk and formed a circularized MAD accreting at a super-Eddington rate. We then inject a TDE stream into the simulation domain as in Curd (2021), allow the stream and pre-existing MAD to interact, and study how the presence of a TDE stream changes the dynamics compared to a typical MAD system. We note that our methods are similar to that of Chan et al. (2019), but they study systems where the disk and stream are misaligned initially and the disk is geometrically thin.

The BH mass is set to $10^6 M_\odot$, though this only sets the units since GRMHD is scale free. We start with a torus of gas in hydrostatic equilibrium threaded by a large-scale poloidal magnetic field and its angular momentum aligned with the BH spin axis (or z -axis). From the torus initial conditions, the magnetorotational instability naturally develops and drives accretion onto the BH, which ultimately drags in magnetic field which saturates at the MAD state. We perform two such initial simulations (one for each BH spin) and evolve this initial stage for $15,000 t_g$, which is long enough for the magnetic field to saturate. We give additional details of the initial torus and time evolution of our initial setup in Appendix B. The simulation state for each BH spin after the initial evolution before stream injection is shown in Figure 2.

To inject the stream, we assume the stream resulted from the disruption of a $1 M_\odot$ star on a parabolic trajectory (eccentricity $e = 1$) around a $10^6 M_\odot$ BH and follow the injection methodology described in Curd (2021) with a few modifications. We reproduce relevant expressions from Curd (2021) below for completeness.

We describe the disruption in terms of the impact parameter, β , which is defined as the ratio between the tidal radius and pericenter separation such that $\beta \equiv R_t/R_p$. We choose $\beta = 4$ for BH spin $a_* = 0$ models and $\beta = 7$ for $a_* = 0.9$. This gives a self-intersection radius (ignoring interaction between the stream and disk) of $\sim 50 r_g$ for all models.

We apply the ‘frozen in’ approximation to estimate the spread in binding energy Stone et al. (2013):

$$\Delta\epsilon \approx 4.3 \times 10^{-4} \frac{m_6^{1/3} m_*^{2/3}}{r_*} c^2. \quad (13)$$

We set the binding energy of the stream to that of the most bound component, $\epsilon_{\text{inj}} = \epsilon_{\text{mb}} = \epsilon_* - \Delta\epsilon/2$. Here ϵ_* is the initial orbital binding energy of the star, which is zero since we assume a parabolic orbit. We note that this is not accurate for late times in a TDE and ϵ of incoming material will slowly approach zero, but we maintain this assumed binding energy for all simulations for simplicity. The orbit of the disrupted star is assumed to be aligned with the equatorial plane of the BH spin vector.

For each simulation we fix \dot{M}_{inj} (and correspondingly ρ_{inj}) to be constant since the simulation time is much shorter than the fallback time. We set the gas temperature $T_{\text{inj}} = 10^5$

Model	a_*	β	\dot{M}_{injd} (\dot{M}_{Edd})	$f_{\rho,0}$	t_{start} ($10^4 t_g$)	t_{end} ($10^4 t_g$)
m00f0.3b4	0	4	1	0.3	0	2
m00f0.003b4	0	4	100	0.003	0	2
m09f1b7A	0.9	7	1	1	0	2
m09f0.1b7A	0.9	7	10	0.1	0	3.5
m09f0.01b7	0.9	7	100	0.01	0	3.5
m09f1b7B	0.9	7	1	1	2	3.5
m09f0.1b7B	0.9	7	10	0.1	2	7

Table 1. Here we describe the relevant parameters of each model presented in this work. Models m09f1b7B and m09f0.1b7B are restarts of m09f0.01b7 from 20,000 t_g with the injection rate lowered to increase the initial density contrast $f_{\rho,0}$ to study how an evolved system changes once self-intersection is weakened.

K, gas pressure $p_{\text{inj}} = k_B T_{\text{inj}} / \mu_{\text{gas}} m_p$ ¹, and injection radius $R_{\text{inj}} = 250 r_g$. Due to resolution limitations, we assume $(H/R)_{\text{inj}} = 0.05$, which subtends only 6 cells in ϑ and 2 cells in φ in our grid. The angular momentum is fixed to the value corresponding to the pericenter radius of the TDE stream $l = \sqrt{2} R_p$, from which we obtain the φ velocity $v^\varphi = l/R_{\text{inj}}$. The total velocity is then set by

$$v_{\text{inj}} = \sqrt{\frac{2}{R_{\text{inj}}} + 2\epsilon_{\text{inj}}}, \quad (14)$$

from which we obtain the radial velocity, $v^r = -\sqrt{(v_{\text{inj}})^2 - (v^\varphi)^2}$. We inject a weak toroidal magnetic field with the stream by setting

$$B_{\text{inj}}^r = \frac{p_{\text{inj}} \beta_{g,\text{inj}}}{\sqrt{g^{r\bar{r}}}} \cos\left(\frac{|\vartheta - \pi/2|}{(H/R)_{\text{inj}}} \pi\right), \quad (15)$$

where $\beta_{g,\text{inj}} = 10^{-3}$ is the ratio magnetic and gas pressure in the injection cells. The other field components are set to $B_{\text{inj}}^\vartheta = B_{\text{inj}}^\varphi = 0$.

4 DEFINITIONS

In this section, we discuss the units adopted throughout the text and provide brief descriptions of quantities used to study the KORAL simulation data.

Throughout this work, we use gravitational units to describe physical parameters. For distance we use the gravitational radius $r_g \equiv GM_{\text{BH}}/c^2$ and for time we use the gravitational time $t_g \equiv GM_{\text{BH}}/c^3$, where M_{BH} is the mass of the BH. Often, we set $G = c = 1$, so the above relations would be equivalent to $r_g = t_g = M_{\text{BH}}$. Occasionally, we restore G and c when we feel it helps to keep track of physical units.

We adopt the following definition for the Eddington mass accretion rate:

$$\dot{M}_{\text{Edd}} = \frac{L_{\text{Edd}}}{\eta_{\text{NT}} c^2}, \quad (16)$$

where $L_{\text{Edd}} = 1.25 \times 10^{38} (M_{\text{BH}}/M_\odot) \text{ erg s}^{-1}$ is the Eddington luminosity, η_{NT} is the radiative efficiency of a thin disk

around a BH with spin parameter a_* (which is often referred to as the Novikov-Thorne efficiency):

$$\eta_{\text{NT}} = 1 - \sqrt{1 - \frac{2}{3r_{\text{ISCO}}}}, \quad (17)$$

and $r_{\text{ISCO}} = 3 + Z_2 - \sqrt{(3 - Z_1)(3 + Z_1 + 2Z_2)}$ is the radius of the Innermost Stable Circular Orbit (ISCO, Novikov & Thorne 1973) in the Kerr metric, where $Z_1 = 1 + (1 - a_*^2)^{1/3} \left((1 + a_*)^{1/3} + (1 - a_*)^{1/3} \right)$ and $Z_2 = \sqrt{3a_*^2 + Z_1^2}$. For $a_* = 0$ and 0.9, the efficiency is $\eta_{\text{NT}} = 5.72\%$ and 15.58%.

We compute the net mass inflow rate as

$$\dot{M}(r) = - \int_0^{2\pi} \int_0^\pi \sqrt{-g} \rho u^r d\vartheta d\varphi. \quad (18)$$

The magnetic flux is computed as

$$\Phi(r) = - \frac{1}{2} \int_0^{2\pi} \int_0^\pi \sqrt{-g} |B^r(r)| d\vartheta d\varphi, \quad (19)$$

where B^r is the radial component of the magnetic field.

The total energy flux (excluding the rest mass flux) is computed as

$$L(r) = - \int_0^{2\pi} \int_0^\pi \sqrt{-g} (T^r_t + \rho u^r) d\vartheta d\varphi. \quad (20)$$

We track the time evolution of the mass accretion rate, magnetic flux, and jet power through unitless quantities evaluated at the BH horizon. We track the accretion of mass onto the BH in each simulation in Eddington units

$$\dot{m} = \frac{\dot{M}(r_H)}{\dot{M}_{\text{Edd}}}. \quad (21)$$

We quantify the magnetic field strength at the BH horizon through the normalized magnetic flux parameter (Tchekhovskoy et al. 2011)

$$\phi = \frac{\Phi(r_H)}{\sqrt{\dot{M}(r_H)}}. \quad (22)$$

For geometrically thick disks the MAD state is achieved once $\phi_{\text{BH}} \sim 40 - 50$ (see e.g. Tchekhovskoy et al. 2011, 2012). Since the majority of the escaping energy leaves the system through the jet in MAD disks, we quantify the jet power via the total efficiency at the BH horizon

$$\eta = \frac{L(r_H)}{\dot{M}(r_H)}. \quad (23)$$

To determine the driving factor for angular momentum transport, we measure the effective viscosity

$$\alpha_{\text{eff}} = \frac{u^r u^\varphi}{c_s^2}, \quad (24)$$

Reynolds viscosity

$$\alpha_{\text{Rey}} = \frac{\hat{T}^{\hat{r}\hat{\varphi}}}{p_b + p_g}, \quad (25)$$

and Maxwell viscosity

$$\alpha_{\text{Max}} = \frac{\hat{T}^{\hat{r}\hat{\varphi}}}{p_b + p_g}. \quad (26)$$

Here $\hat{T}^{\hat{r}\hat{\varphi}}$ is the average orthonormal r, φ component of the stress-energy tensor measured in the fluid frame, c_s is the sound speed, and $p_b = b^2/2$ is the magnetic pressure. Note

¹ Here k_B is the Boltzmann constant, m_p is the mass of a proton, and μ_{gas} is the mean molecular weight assuming Solar metallicity.

that we have taken advantage of the fact that the stress-energy tensor can be broken into gas (Reynolds) and magnetic (Maxwell) components. That is we write Equation 12 strictly in terms of the gas or magnetic components.

We compute the eccentricity at each grid point via

$$e = \sqrt{1 + 2\epsilon l^2}, \quad (27)$$

where $\epsilon = -(u_t + 1)$ is the binding energy and $l = u_\varphi$ is the angular momentum.

To quantify the orientation of the disk and jet (or corona/funnel), we first use the magnetization to divide the fluid into 'disk' ($\sigma < 1$) and 'jet' ($\sigma \geq 1$). In simulations where there is no spin, this is not a true jet since there is no mechanism to accelerate the gas to relativistic speeds. Nevertheless, this region is likely to be low optical depth and represents where X-rays are likely to escape.

Note that we transform quantities from spherical polar to cartesian coordinates $x^i = (x, y, z)$ to describe the position and angular momentum of the fluid in the following paragraphs. The angular momentum of the BH is aligned with the z -axis, so

$$J_{\text{BH}}^i = (0, 0, a_{\text{BH}}M). \quad (28)$$

Since this term cancels when computing the tilt and precession and is meaningless for a Schwarzschild BH, we only show it here for completeness. We derive the angular momentum of each cell in the disk using the stress energy tensor transformed to Cartesian coordinates

$$S^i = [i j k] x^j T_{\text{Cart}}^{0k}, \quad (29)$$

where the brackets denote the antisymmetric Levi-Cevita tensor. We then find the shell integrated, density weighted angular momentum components

$$J^i = \frac{\int_0^{2\pi} \int_0^\pi \sqrt{-g} w_{\text{disk}}(\sigma) \rho S^i d\vartheta d\varphi}{\int_0^{2\pi} \int_0^\pi \sqrt{-g} w_{\text{disk}}(\sigma) \rho d\vartheta d\varphi}. \quad (30)$$

In the above expression, the term

$$w_{\text{disk}}(\sigma) = \begin{cases} 1, & \sigma < 1 \\ 0, & \sigma \geq 1 \end{cases} \quad (31)$$

is used to only include the disk in integration. We then define the tilt angle relative to the BH spin (or z -axis in the zero spin case) as a function of radius

$$\mathcal{T}_{\text{disk}}(r) = \arccos \left[\frac{J^z}{\sqrt{(J^x)^2 + (J^y)^2 + (J^z)^2}} \right]. \quad (32)$$

We also obtain the precession angle relative to the y -axis

$$\mathcal{P}_{\text{disk}}(r) = \arccos \left[\frac{J^y}{\sqrt{(J^x)^2 + (J^y)^2}} \right]. \quad (33)$$

In aligned systems, the precession angle is not a useful quantity, but once tilt sets in it can show whether the disk and jet precess together.

For the jet, we derive a position based angle. We start by finding the σ weighted mean position for the top and bottom jet at each radius

$$x_{\text{jet,top}}^i = \frac{\int_0^{2\pi} \int_0^{\pi/2} \sqrt{-g} w_{\text{jet}}(\sigma) \sigma x^i d\vartheta d\varphi}{\int_0^{2\pi} \int_0^{\pi/2} \sqrt{-g} w_{\text{jet}}(\sigma) \sigma d\vartheta d\varphi}, \quad (34)$$

$$x_{\text{jet,bot}}^i = \frac{\int_0^{2\pi} \int_{\pi/2}^\pi \sqrt{-g} w_{\text{jet}}(\sigma) \sigma x^i d\vartheta d\varphi}{\int_0^{2\pi} \int_{\pi/2}^\pi \sqrt{-g} w_{\text{jet}}(\sigma) \sigma d\vartheta d\varphi}. \quad (35)$$

In both expressions, the term

$$w_{\text{jet}}(\sigma) = \begin{cases} 0, & \sigma < 1 \\ 1, & \sigma \geq 1 \end{cases} \quad (36)$$

is used to explicitly exclude the disk from calculations. We then calculate a tilt and precession angle based on the mean position. For example, the top jet's tilt and precession are calculated as

$$\mathcal{T}_{\text{jet,top}}(r) = \arccos \left[\frac{z_{\text{jet,top}}}{\sqrt{(x_{\text{jet,top}})^2 + (y_{\text{jet,top}})^2 + (z_{\text{jet,top}})^2}} \right], \quad (37)$$

and

$$\mathcal{P}_{\text{jet,top}}(r) = \arccos \left[\frac{y_{\text{jet,top}}}{\sqrt{(x_{\text{jet,top}})^2 + (y_{\text{jet,top}})^2}} \right]. \quad (38)$$

The same expressions are used for the bottom jet except with the mean coordinates $x_{\text{jet,bot}}^i$. For both the disk and jet, we report the average tilt and precession angles over $10 \leq r/r_g \leq 100$.

We quantify the jet opening angle by computing the solid angle it subtends in a flat spacetime:

$$\Omega_{\text{jet,top}}(r) = \int_0^{2\pi} \int_0^{\pi/2} w_{\text{jet}}(\sigma) \sin(\vartheta) \cos(\vartheta) d\vartheta d\varphi \quad (39)$$

$$\Omega_{\text{jet,bot}}(r) = - \int_0^{2\pi} \int_{\pi/2}^\pi w_{\text{jet}}(\sigma) \sin(\vartheta) \cos(\vartheta) d\vartheta d\varphi. \quad (40)$$

Note the minus sign in Equation 40 is to account for the negative introduced by $\cos(\vartheta)$. We compute an average solid angle

$$\Delta\Omega(r) = \frac{\Omega_{\text{jet,top}}(r) + \Omega_{\text{jet,bot}}(r)}{2}. \quad (41)$$

We relate this to the mean jet width under the assumption of a conical geometry

$$\mathcal{W}(r) = r \sin \left(\arccos[1 - \Delta\Omega(r)/2\pi] \right). \quad (42)$$

5 RESULTS

5.1 Stream/Disk Dynamics

We show the large scale structure of models with $f_\rho = 0.01, 0.1, 1$ and $a_* = 0.9$ in Figure 3 (m09f1b7A, m09f0.1b7A, m09f0.01b7). When $f_\rho = 0.01$, the ram pressure from the disk is negligible, and the system evolves much like disk formation simulations initialized with no initial disk (Sadowski et al. 2016; Curd 2021). The stream dissipates a negligible amount of orbital energy on its way to pericenter, where it goes through a nozzle shock due to vertical compression and self-intersects at roughly the self-intersection radius (See bottom left panel in Figure 3 and bottom right panel in Figure 4). Similar to Curd (2021), the nozzle shock is poorly resolved,

so we do not discuss it throughout this work. Bound and unbound gas is produced by the self-intersection shock, some of which falls in and makes an accretion disk while the rest flows out and interacts with the jet and outer medium. The material which forms the accretion disk maintains a high eccentricity (See bottom right panel in Figure 5). Despite the low magnetic field strength injected with the stream, the forming disk maintains a strong magnetic field due to the pre-existing field being anchored to smaller radii by inflowing material (See bottom right panel in Figure 3). Similar to the magnetized disk formation simulations in Curd (2021), the magnetic field in material which has gone through the self-intersection shock becomes highly disordered and turbulent. However, as we discuss later, the poloidal magnetic flux inside the self-intersection radius remains trapped and the field in the inner accretion disk remains ordered. The outflowing part is launched with velocity $\sim 0.1c$ and produces an asymmetrical ram pressure on the jet since it is quasi-spherical. This results in a force in the $-x$ direction. We describe how this affects the disk and jet evolution in Section 5.4.1.

With $f_\rho = 0.1$, we observe significant slowing of the stream on its way to pericenter, but it is not completely stopped by the disk (See middle left panel in Figure 3 and bottom left panel in Figure 4). As a consequence, the pericenter radius is shifted outward radially significantly and the self-intersection has far less kinetic energy available for dissipation. No quasi-spherical outflow is produced as a result. This may be due to the shock weakening due to poorer resolution at larger radii. However, this result is not unreasonable since the energy and velocity of the self-intersection outflow is expected to rapidly drop off with increasing radius since the stream self-intersects at roughly the orbital velocity. We again find a highly eccentric accretion disk forms, but we note a slight decrease in eccentricity compared with the $f_\rho = 0.01$ model due to the dissipation of orbital energy as the stream interacts with the disk (See bottom left panel in Figure 5). Since there is no self-intersection outflow, the magnetic field in the outer accretion disk is less turbulent. We again find anchoring of poloidal magnetic field to the BH by the inflowing material.

With $f_\rho = 1$, the ram pressure exerted on the stream by the disk is large enough to halt the stream before it reaches pericenter. Instead, the stream is observed to mix with the accretion disk (See top panel in Figure 3). This can clearly be seen in the velocity which closely resembles the initial MAD disk (See top panels in Figure 4). Interestingly, the stream does add eccentricity to the disk as the inflowing material reaches $e > 0.7$. The field structure closely resembles a standard MAD accretion disk (e.g. bottom panel in Figure 2) since the stream has little effect on the disk.

The dynamics for a given f_ρ are similar in the $a_* = 0$ models. Videos of each simulation can be seen in our [YouTube playlist](#).

5.2 TDE Disks Maintain Magnetic Flux and Jets

We show the accretion rate, normalized magnetic flux, and efficiency at the BH horizon in Figure 6. In all models save m09f0.01b7, the accretion rate drops from about 10 to 1 Edgington. This is due to a drop in density around the BH as the disk spreads viscously and mass is consumed by the BH. Surprisingly, there is little difference in accretion history as we vary f_ρ except in m09f0.01b7 which shows elevated ac-

cretion once the disk tilts, an effect we describe in the next section.

In all models, a MAD or semi-MAD state is maintained. Despite the high eccentricity, magnetic field is successfully contained and does not rapidly diffuse from the horizon. This is a genuinely new result and is a bit of a surprise since Curd (2021) found negligible poloidal flux accumulation when the field comes from the stream even with a favorable field configuration. Our results indicate that once poloidal flux reaches the BH, regardless of how it was obtained (i.e. fossil disk or a dynamo effect), the chaotic and eccentric disk can anchor it to the BH. We note that while m09f0.01b7 showed a decrease in normalized magnetic flux, the total magnetic flux given by Equation 19 remains roughly the same. The decrease in normalized magnetic flux is due to additional accretion driven by strong shocks once the tilt sets in. See discussion in Section 5.4.1.

We treat the efficiency as measured at the horizon as a proxy for the outgoing jet power. In all models with $a_* = 0.9$ we find $\eta \approx 100 - 400\%$ while the magnetic flux remains MAD ($\phi \gtrsim 50$). Ultimately, the jet power at larger radii may decrease especially in cases where the self-intersection outflow is strong, and the jet may interact with the disk and outflow. In addition, instabilities in the jet disk interface can lead to additional dissipation of jet power (Chatterjee et al. 2019). For models with spin $a_* = 0$, the efficiency remains much lower at $\sim 2 - 6\%$ since there is no jet.

5.3 Magnetic Stresses are Subdominant

To quantify the contribution to angular momentum transport from hydrodynamic and magnetic processes, we compute a radius-weighted average of α_{eff} , α_{Rey} , and α_{Max} in the disk ($\sigma < 1$) from $r_H < r < 100r_g$ at $t = t_{\text{end}}$ ². We employ radius-weighting instead of density-weighting to incorporate part of the outer disk where shocks are present into the calculation.

We show the average viscosity in Figure 7 as a function of f_ρ . We find that the effective and Reynolds viscosity both decline as a function of f_ρ . Meanwhile, the Maxwell viscosity is similar across all values of f_ρ with $\alpha_{\text{Max}} \lesssim 10^{-3}$. At all values of f_ρ , the effective viscosity and the Reynolds viscosity are larger than the Maxwell viscosity. At $f_\rho \lesssim 0.01$, the effective viscosity is more than an order of magnitude larger than the Reynolds viscosity which suggests shocks dominate transport at this stage of a TDE. We observe that at $f_\rho \gtrsim 0.1$, the effective and Reynolds viscosity are of roughly the same magnitude which suggests a transition to turbulent transport.

Our findings at $f_\rho \lesssim 0.1$ are similar to Sadowski et al. (2016) who found even after a disk formed, the Maxwell viscosity remained subdominant by at least an order of magnitude. At $f_\rho \gtrsim 1$, the viscosity resembles some of the MAD disks in McKinney et al. (2012) which also showed a larger Reynolds viscosity than Maxwell viscosity in spite of the powerful poloidal magnetic fields.

² We have verified that the viscosity behaves the same across time and the qualitative properties shown in Figure 7 are not effected by our choice of time to perform the measurement.

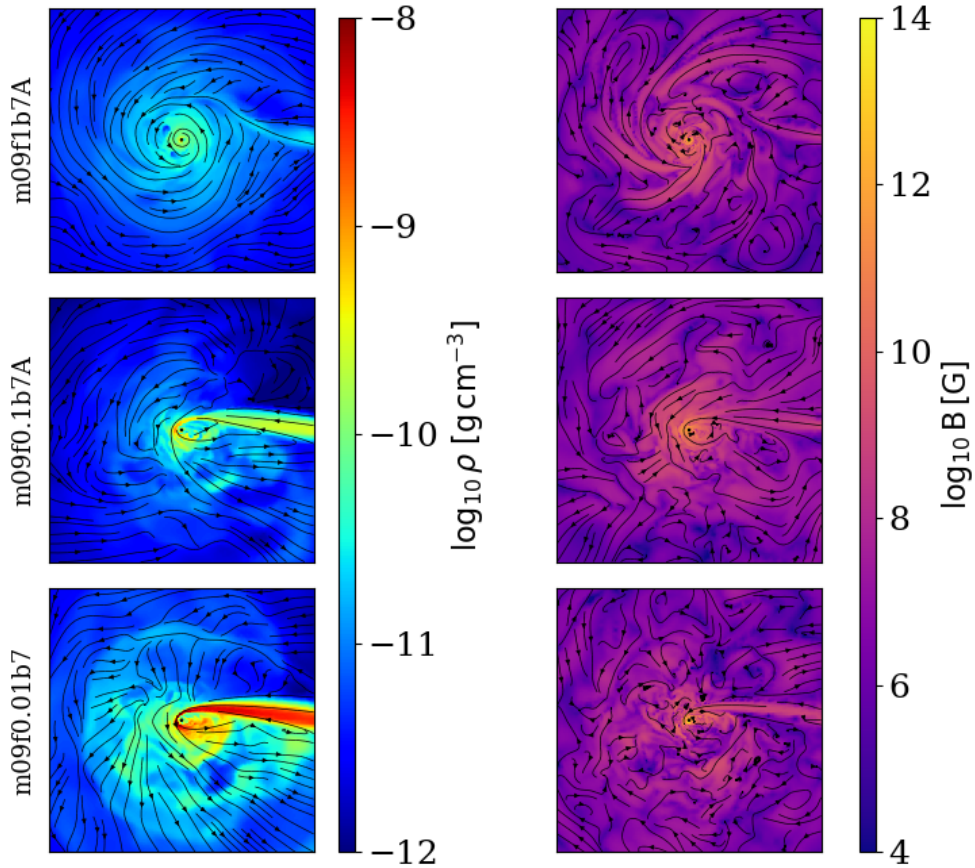


Figure 3. Here we show the gas density (colors, left panels), velocity field (stream lines, left panels), magnetic field strength (colors, right panels), and magnetic field (stream lines, right panels) for an equatorial slice of each of the $a_* = 0.9$ models for $f_p = 0.01$ (bottom row), 0.1 (middle row), 1 (top row). Each figure spans a region of $480r_g \times 480r_g$ centered around the BH. We describe the figure in [Section 5.1](#).

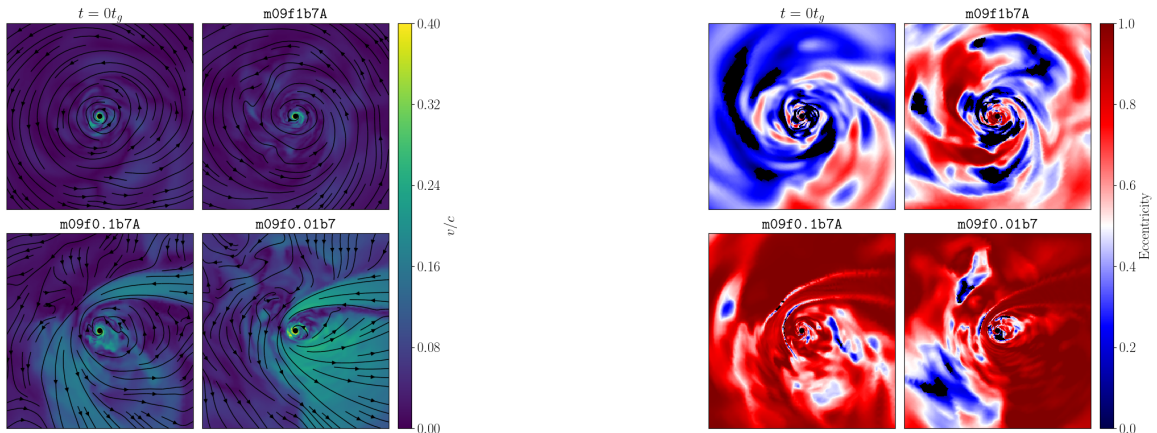


Figure 4. Here we show the velocity (colors) and velocity field vector (stream lines) for an equatorial slice of each of the $a_* = 0.9$ models for $f_p = 0.01$ (bottom right), 0.1 (bottom left), 1 (top right). We also show the velocity field for the initial conditions on the top left for comparison. Each panel shows in $120r_g \times 120r_g$ region centered around the BH. See [Section 5.1](#) for a description of the figures.

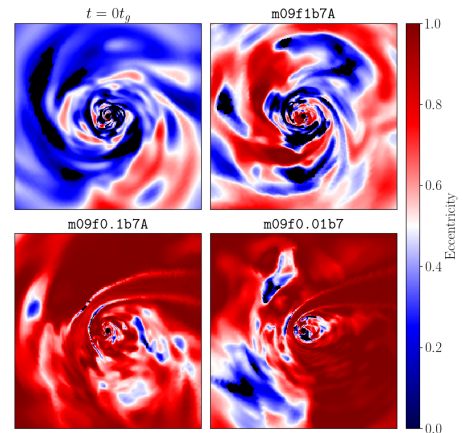


Figure 5. Here we show the eccentricity (colors) for an equatorial slice of each of the $a_* = 0.9$ models for $f_p = 0.01$ (bottom right), 0.1 (bottom left), 1 (top right). We also show the eccentricity for the initial conditions on the top left for comparison. Each figure spans a region similar to [Figure 4](#). See [Section 5.1](#) for a description of the figures.

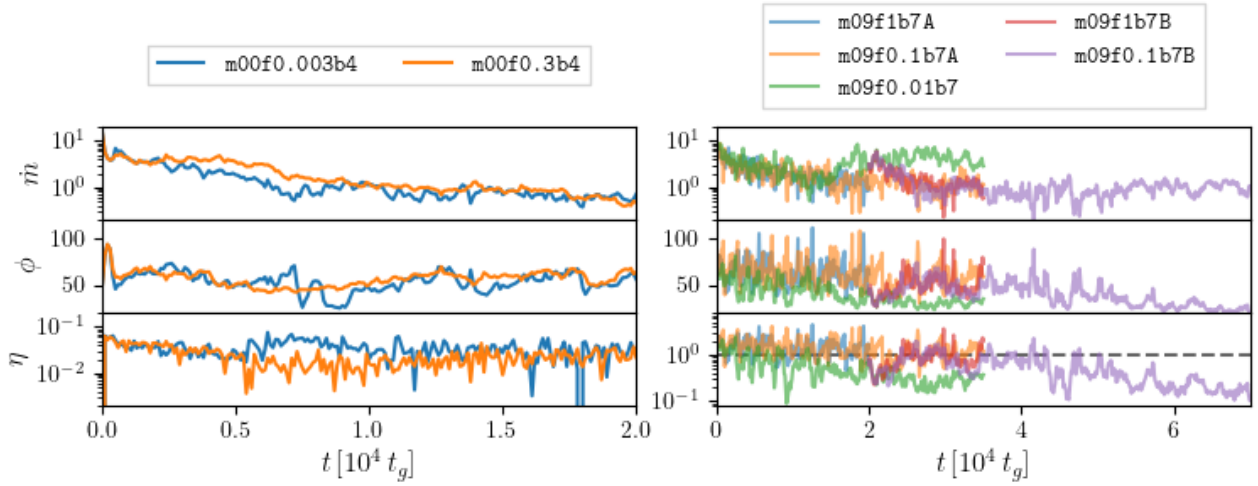


Figure 6. We show the mass accretion rate (top row), normalized magnetic flux at the BH horizon (middle row), and efficiency (bottom row) for each of the $a_* = 0$ (left column) and $a_* = 0.9$ (right column) models. Each model shows an initial decrease in the mass accretion rate as the injected stream interacts with the disk. As we discuss in Section 5.2, this is due to the density in the disk decreasing due to viscous spreading and mass accretion. In each model we find $\phi > 20$, which confirms that TDE disks can maintain a strong poloidal field. For the models where no tilt instability sets in, a MAD flux of $\phi > 50$ is maintained and a powerful jet with $\eta \approx 100 - 400\%$ is launched when $a_* = 0.9$. As expected, no jet is launched when $a_* = 0$ and we find similar η for both of the $a_* = 0$ models.

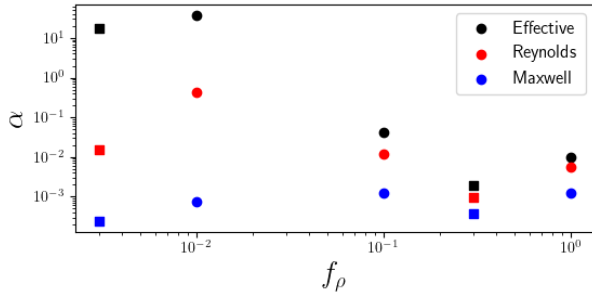


Figure 7. Here we show the radius-weighted viscosity as computed in Section 5.3 as a function of f_ρ . We indicate $a_* = 0$ models as squares and $a_* = 0.9$ models as circles.

5.4 Disk and Jet Tilt Evolution

5.4.1 Low Density Contrast Jetted Model: $f_\rho = 0.01$

At the onset of stream injection, since the stream is substantially denser than the pre-existing MAD disk with $f_\rho = 0.01$, the stream is largely unperturbed by the disk material on its path towards pericenter. Subsequently, the stream precesses and violently self-intersects with itself at the self-intersection radius.

Between $t = 0 - 0.7 \times 10^4 t_g$, the self-intersection outflow begins to tilt the jet and we measure tilt angles for both the top and bottom jet of $\sim 10^\circ - 20^\circ$. During this initial stage, the disk remains aligned with the BH spin. Between $t = 0.7 - 1.2 \times 10^4 t_g$, the disk tilt begins to increase until it roughly equals the tilt angle of the top and bottom jets. During this stage, the precession angle oscillates wildly, in part due to the initial tilt angle of zero.

For $t > 1.2 \times 10^4 t_g$, the tilt of the top jet and disk continue to grow until $\mathcal{T}_{\text{jet,top}} \sim 30^\circ$ and $\mathcal{T}_{\text{disk}} \sim 23^\circ$. In a typical tilted MAD disk system, the jet acts to align the inner accretion

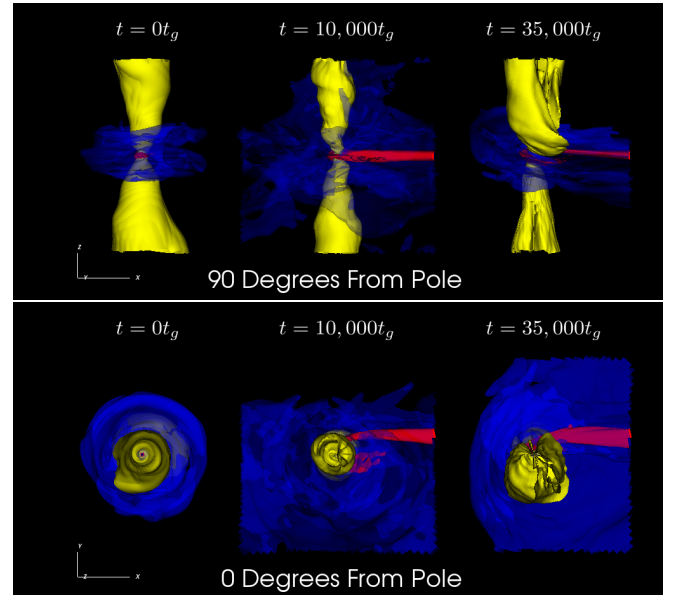


Figure 8. Volume renderings of a $200r_g \times 200r_g$ region of model m09f0.01b7 showing the stream/disk (red), outer disk/outflow (blue), and jet (yellow) viewed edge on (top panel) and viewed down the jet axis (bottom panel). We show times in $t = 0t_g$ (left), $t = 10,000t_g$ (middle), $t = 35,000t_g$ (right). The outflow pushes on the jet laterally and begins to tilt the jet. This ultimately leads to a tilted disk and jet in the final snapshot.

disk with the BH spin. However, once the disk tilt begins to grow in m09f0.01b7, it is unable to realign with the BH spin due to already tilted disk material adding angular momentum at the self-intersection radius. This sets up a tilted system which is shown to be stable for at least the duration of the simulation. Interestingly, the jet precession angle does not show strong variability after the disk tilts. Instead the top

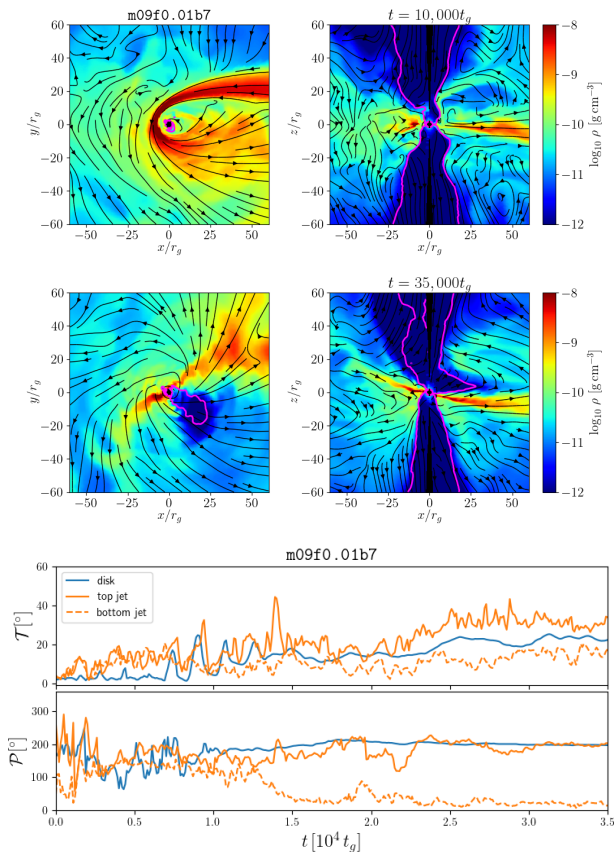


Figure 9. *Top two rows:* Gas density (colors), velocity (streamlines), and jet boundary ($\sigma = 1$, pink line) for m09f0.01b7. We show an equatorial slice (left) and vertical slice (right) spanning a region of $120r_g \times 120r_g$ centered on the BH. Snapshots are shown during the initial self-intersection ($t = 10^4 t_g$, first row), and at the end of the simulation after the tilt has set in (second row). *Bottom two rows:* We show the tilt and precession angle for the disk and top/bottom jet over the evolution of the simulation. As the stream flows in, a quasi-spherical outflow begins to push on the jet and we see the jet tilt increase initially. At around $t = 0.6 \times 10^4 t_g$, the jet begins to perturb the disk and we observe a steady increase in the disk tilt until it roughly aligns with the jet, after which the tilt in both the disk and jet increases until they settle around a rough equilibrium state at $t = 2.5 \times 10^4 t_g$. Once the disk tilts, a feedback cycle begins due to self-intersection and magneto-spin alignment cannot realign the inner disk. The precession angle prior to the tilt setting in is not a meaningful quantity since the system is initially aligned with the BH spin. Once the system tilts, the disk and top jet share the same precession angle and we do not observe much variability in the precession. The bottom jet points in the opposite direction and is roughly 180° out of phase with the top jet.

and bottom jets show nearly constant precession angles that are roughly 180° out of phase at $t > 2.3 \times 10^4 t_g$.

Volume renderings of the evolution are shown in Figure 8. Equatorial and poloidal slices as well as the full time evolution of the tilt and precession angles are shown in Figure 9.

5.4.2 Medium Density Contrast Jetted Model: $f_\rho = 0.1$

Since this model has an intermediate density contrast, the stream is still able to flow towards the BH. However, it is significantly perturbed and the pericenter radius is shifted

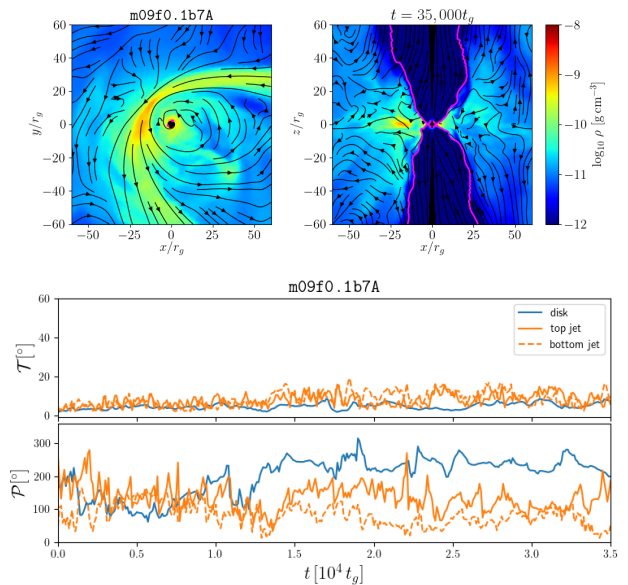


Figure 10. *Top row:* Here we show the same quantities as the top three rows in Figure 9, but for model m09f0.1b7A. As we discuss in Section 5.4.2, the stream loses orbital energy on its path to pericenter and the self-intersection outflow is significantly weakened which leads to a weaker perturbation on the jet. We note that the jet profile is less smooth than in the initial state (top panel in Figure 9) due to asymmetry in the disk structure induced by the interaction with the stream. *Bottom two rows:* The weak perturbation on the jet leads to a non-zero tilt measurement. However, both the disk and jet maintain low tilts with $\mathcal{T} < 10^\circ$, which confirms that strong self-intersection is needed to induce strong interaction between the jet and disk. The top and bottom jet maintain precession angles which are roughly in-phase and oscillate over time, which is typical of spin aligned MAD disks.

slightly outward, which also increases the self-intersection radius. This leads to a substantially weakened self-intersection and self-intersection outflow. As a result, the jet is only slightly perturbed by the outflow and we find that the jet remains stable with $\mathcal{T} \lesssim 10^\circ$ and the disk remains aligned with the BH spin throughout the entire evolution. The precession angle is not meaningful here due to the near perfect alignment. See Figure 10 for visualizations and the time evolution.

5.4.3 High Density Contrast Jetted Model: $f_\rho = 1$

In this model, the density contrast is large enough that the stream experiences extreme ram pressure from the accretion disk and is halted at $r \sim 50 - 100r_g$. The stream material never reaches pericenter and instead mixes in with the pre-existing disk. Consequently, the system resembles a standard MAD ADAF and neither the jet or disk show large changes in their tilt. Again, the precession angle is not meaningful here due to the near perfect alignment. This evolution is depicted in Figure 11.

5.4.4 Restarts of m09f0.01b7 with Higher Density Contrast

For model m09f1b7B, we perform a restart of m09f0.01b7 at $t = 2 \times 10^4 t_g$ with f_ρ instantaneously increased from 0.01 to

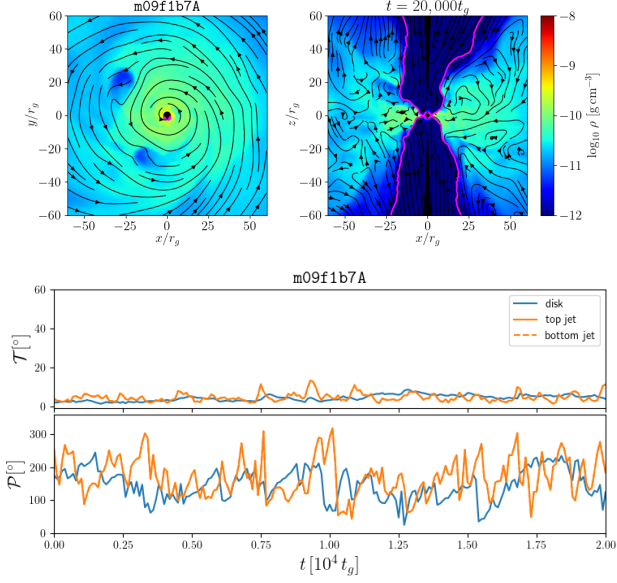


Figure 11. The same as Figure 10, but for model m09f1b7A. Since the stream is halted by the pre-existing disk, no self-intersection outflow occurs. Subsequently, the jet and disk are approximately aligned with the BH spin throughout the entire simulation. Interestingly, the added turbulence to the system during the interaction with the stream appears to perturb the jet boundary compared to the initial state. Note the precession angle of the disk is not a useful quantity since the disk is aligned with the BH.

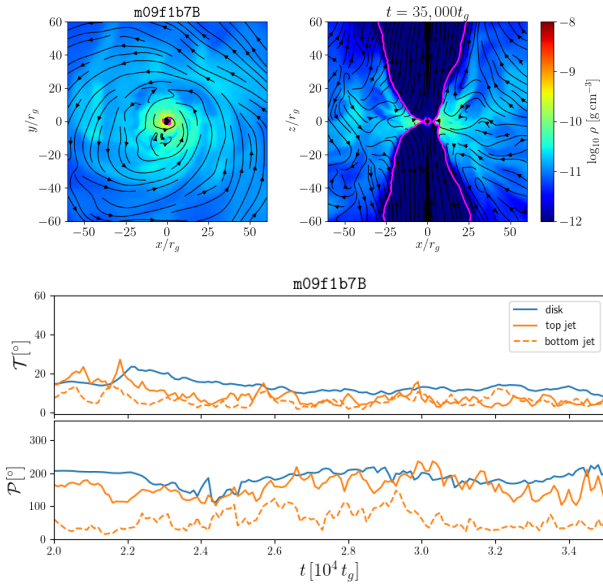


Figure 12. The same as Figure 10, but for model m09f1b7B which is a restart of m09f0.01b7 at $t = 2 \times 10^4 t_g$. f_ρ is instantaneously increased from 0.01 to 1 at the start of the simulation. Because the stream is halted by the disk due to the change in density contrast, the self-intersection ceases shortly after we start the simulation. Without the added perturbation from a self-intersection outflow, the jet realigns with the z-axis and magneto-spin alignment rapidly realigns the disk with the BH spin. Interestingly, the top and bottom jet remain approximately 180° out of phase even after self-intersection ceases.

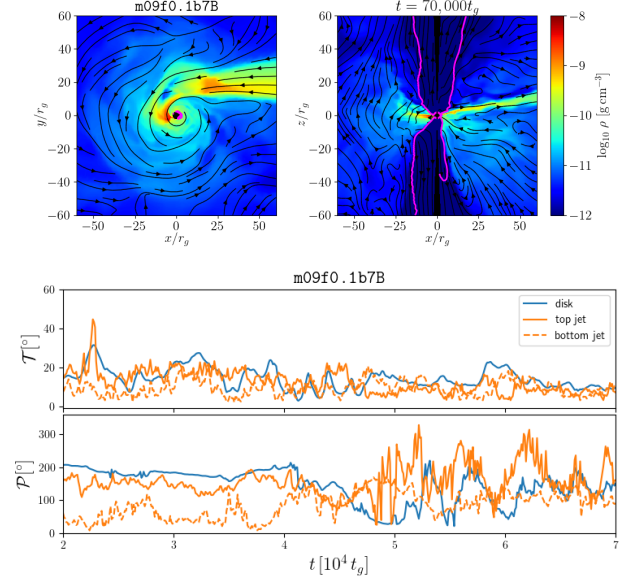


Figure 13. The same as Figure 10, but for model m09f0.1b7B which is a restart of m09f0.01b7 at $t = 2 \times 10^4 t_g$. f_ρ is instantaneously increased from 0.01 to 0.1 at the start of the simulation. Since the change in density contrast is milder than m09f1b7B, the stream manages to penetrate the disk, but loses a substantial amount of orbital energy similar to model m09f0.1b7A. As a result, the self-intersection outflow persists, but is much weaker. The tilt of the jet and disk slowly decreases over the course of the simulation until it was observed to reach a rough equilibrium of about 10° . Although magneto-spin alignment is able to realign much of the inner system, filaments of tilted material linger in the disk which may contribute to the residual tilt in the system as well as the wild precession observed in the jet at late times.

1. The self-intersection is rapidly halted due to the increased density contrast and the jet subsequently realigns with the BH spin. The tilt of the disk remains slightly elevated above the tilt of the jet. This is due to the density weighting applied in Equation 30, which gives larger weighting to higher density remnants of the tilted gas which is still in the simulation domain. However, as can be seen in Figure 12, the inner disk is able to realign with the BH spin by the end of the simulation. We expect in a physical scenario the system will have time to adjust and the disk tilt should completely realign with the BH spin similar to the jet.

For model m09f0.1b7B, we also perform a restart of model m09f0.01b7 at $t = 2 \times 10^4 t_g$, but with f_ρ instantaneously increased from 0.01 to 0.1. Similar to m09f0.1b7A, the stream is only perturbed from its orbit and the self-intersection still persists, but is weakened as a result. With weaker ram pressure acting on the jet, the jet and disk begin to realign with the BH spin. However, this process is much slower than in model m09f1b7B, and we find that the disk and jet tilt are highly variable until finally decreasing until they settle at $\mathcal{T} \sim 10^\circ$ by the end of the simulation (see Figure 13). The total run time of the simulation (see Table 1) corresponds to only roughly three days for a $10^6 M_\odot$ BH which suggests, assuming rapid transitions in the density contrast, that the tilt can evolve rapidly enough to explain features such as jet shut-off as we discuss later in this work.

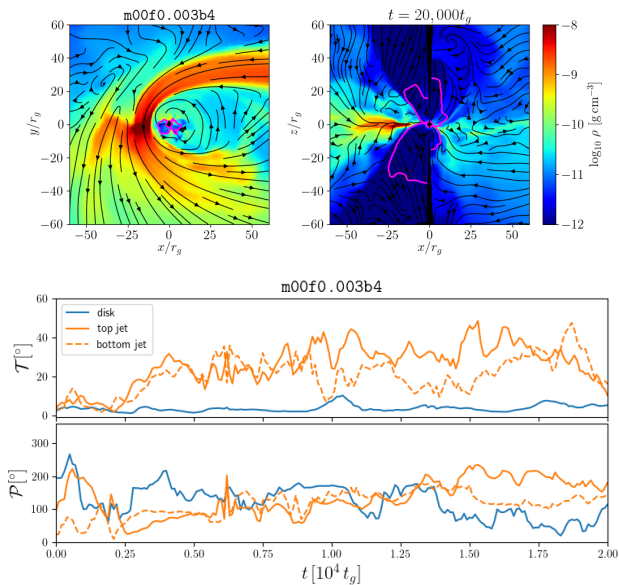


Figure 14. The same as Figure 10, but for model m09i100b4. Note we show the initial state in the top row and the final state of the simulation in the bottom row. Since there is no jet, the corona is observed to tilt by $\mathcal{T} > 20^\circ$ due to the self-intersection outflow. However, the disk tilt remains approximately aligned with the BH spin. This confirms that a jet is necessary to induce a tilt instability in MAD TDE disks.

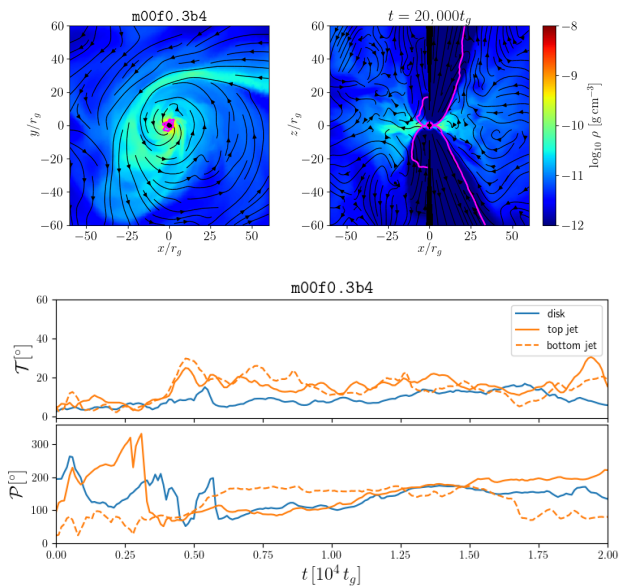


Figure 15. The same as Figure 10, but for model m09i1b4. Due to the higher density contrast, the stream loses orbital energy on its way to pericenter, and the self-intersection outflow is negligible. Surprisingly, we measure a nonzero tilt for the corona and disk. We believe this is due to asymmetry introduced to the system by the stream in the absence of magneto-spin alignment and a strong jet.

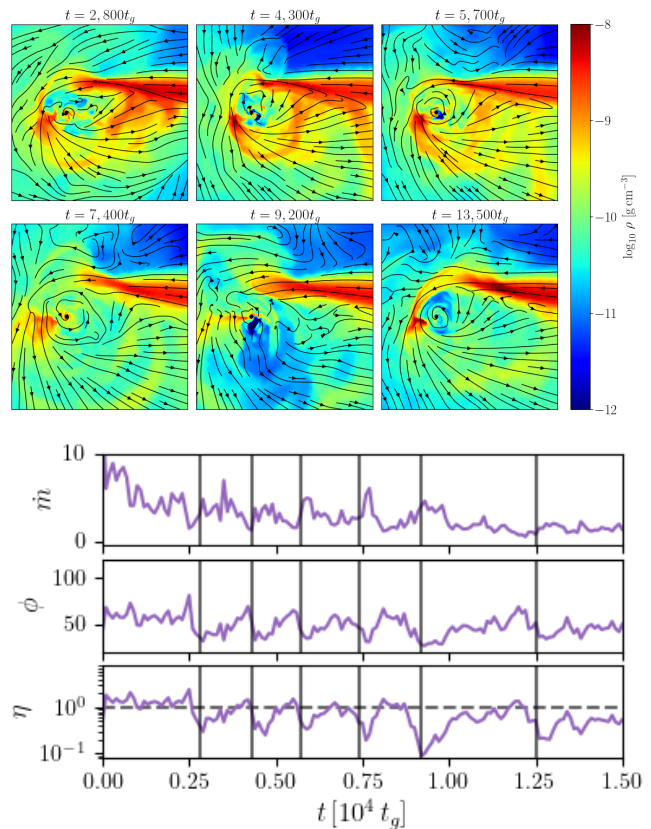


Figure 16. Here we show snapshots of violent self-intersection events in model m09f0.01b7 (first and second row). Colors indicate gas density and stream lines indicate gas velocity. We also show the mass accretion rate (third row), magnetic flux threading the BH (fourth row), and jet efficiency (fifth row). Vertical gray lines correspond to the same times as the snapshots shown in the first and second rows, 2, 800, 4, 300, 5, 700, 7, 400, 9, 200, and 13, 500 t_g , respectively. The violent self-intersections are accompanied by a drop in magnetic flux and jet power. We also note a small increase in mass accretion rate, which is less dramatic than the change in magnetic flux and jet efficiency.

5.4.5 Non-Jetted Models

For the low density contrast model (m00f0.003b4), the initial evolution of the streams is similar to that of model m09f0.01b7. The self-intersection and self-intersection outflow result in a ram pressure which tilts the jet region. However, as there is no true jet since $a^* = 0$, the jet region that we measure may be thought of as a corona. As shown in Figure 14, the corona becomes substantially tilted with $\mathcal{T} \sim 20^\circ - 40^\circ$. The disk remains perfectly aligned with the BH spin throughout the entire evolution. This demonstrates that a powerful jet is responsible for the tilt instability that we observe in m09f0.01b7.

For the low density contrast model (m00f0.3b4), the stream is perturbed due to its interaction with the pre-existing disk, similar to m09f1b7A. However, we find that the disk tilt increases slightly over the course of the simulation ($\mathcal{T} \lesssim 10^\circ$, see Figure 15). The corona attains a tilt of $\mathcal{T} \sim 20^\circ$. This is due to asymmetry introduced to the system as the stream interacts with the disk. Since the magnetic field is strong, and stream material cannot steadily feed aligned material

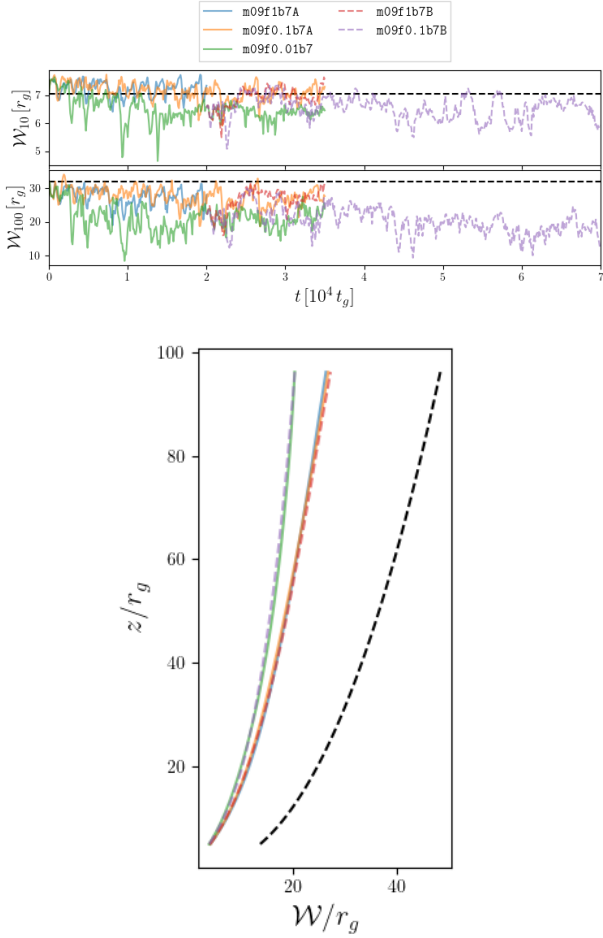


Figure 17. We show the mean jet width at $r = 10r_g$ (W_{10} , top panel) and $r = 100r_g$ (W_{100} , middle panel) as a function of time for each model. In the bottom panel we show the mean jet width as a function of z and time averaged over $t_{\text{start}} + 5000t_g$ to t_{end} . We also show the jet profile for the $a_* = 0.9$ model from Narayan et al. (2022) (dashed black line). We describe the figures in Section 5.6.

to the inner disk, the tilted corona is capable of tilting the disk. Unlike model m09f1b7A, magneto-spin alignment does not counteract any induced tilt. Tilt induction in a MAD around a non-spinning BH was also demonstrated by Ressler et al. (2020) in the context of a stellar wind fed model of Sagittarius A*, suggesting tilt induction may be common in MAD disks around non-spinning BHs that are fueled by asymmetrical inflows.

5.5 Violent Self-Intersections and Variability

For the first $15,000t_g$ of model m09f0.01b7, we identify six complete stream disruptions at times (2,800, 4,300, 5,700, 7,400, 9,200, 13,500) t_g as shown in Figure 16. These correspond to a temporal separation of (1500, 1400, 1700, 1800, 3300) t_g . Assuming a Keplerian orbit, this corresponds to an orbital radius of (38, 37, 42, 43, 65) r_g . These are similar to the self-interaction radius of $\sim 50r_g$, which is to be expected in the case of a

feedback loop caused by angular momentum transfer during self-intersection (Sadowski et al. 2016; Curd 2021).

Here we find that not only does the mass accretion rate vary during these events, but the magnetic flux threading the BH drops from $\phi_{\text{BH}} \sim 60$ to ~ 40 . Since the disk is MAD and the BH is rapidly rotating, this will inevitably lead to flaring behaviour. Indeed, we see the total efficiency drop from $\sim 100\%$ at the peaks to $10 - 50\%$ at the minima. We discuss how our model can be applied to the variability in jetted TDEs like *Swift* J1644+57 in Section 6.

5.6 Jet Collimation

We measure the mean jet width at $r = 10r_g$ (W_{10}) and $r = 100r_g$ (W_{100}) as a function of time following Equation 42 in Figure 17. The jet width shows oscillations as a function of time due to the highly variable magnetic flux. This is typical of a MAD disk, but here we are focused on the average behavior of the jet.

For model m09f0.01b7, the self-intersection outflow causes substantial collimation. The velocity stream lines in the right middle panel of Figure 9 show high density material sometimes flowing completely in the $-x$ direction which will provide substantial ram pressure on the jet. We see a decrease of roughly $10r_g$ in the jet width measured at $100r_g$ compared to the initial jet.

For models m09f1b7A and m09f0.1b7A, the jet width at $r = 10r_g$ is similar to that of the initial jet prior to injection due to the weakening of the self-intersection outflow. However, we do observe slightly more collimation at $r = 100r_g$ compared to the initial jet, perhaps due to changes in the outflow properties when the stream interacts with the disk. For instance, the velocity stream lines in Figure 11 and Figure 10 show flows towards the jet axis, which are not present in the initial jet (see top panel of Figure 9). This may lead to more collimation in TDE jets as they propagate outwards compared to a standard MAD; however, we limit ourselves to measuring the jet profile for $r \leq 100r_g$ due to poor angular resolution of the jet at larger radii.

For model m09f1b7B, the self-intersection ceases due to the increased f_p , the jet width returns to near the initial value within $\sim 5000t_g$. However, model m09f0.1b7B shows a much narrower jet when compared with model m09f0.1b7A. This is not due to the self-intersection outflow, but the magnetic flux dropping off towards the end of the simulation.

We also time average the jet width from $t_{\text{start}} + 5000t_g$ to t_{end} (see bottom panel in Figure 17). We find similar jet profiles for all models with weak self-intersection outflows (m09f1b7A, m09f0.1b7A, m09f1b7B). Model m09f0.1b7B is similar to model m09f0.01b7, but again this is due to a decrease in magnetic flux and not a result of the self-intersection outflow. We compare our results with the jet profile for the $a_* = 0.9$ model from Narayan et al. (2022). We find that our initial conditions result in a slightly narrower jet, but the profile appears to be quite similar for the models with weak self-intersection.

5.7 Gas Temperature

We estimate the gas temperature in the disk by accounting for radiation under the assumption that the disk is optically

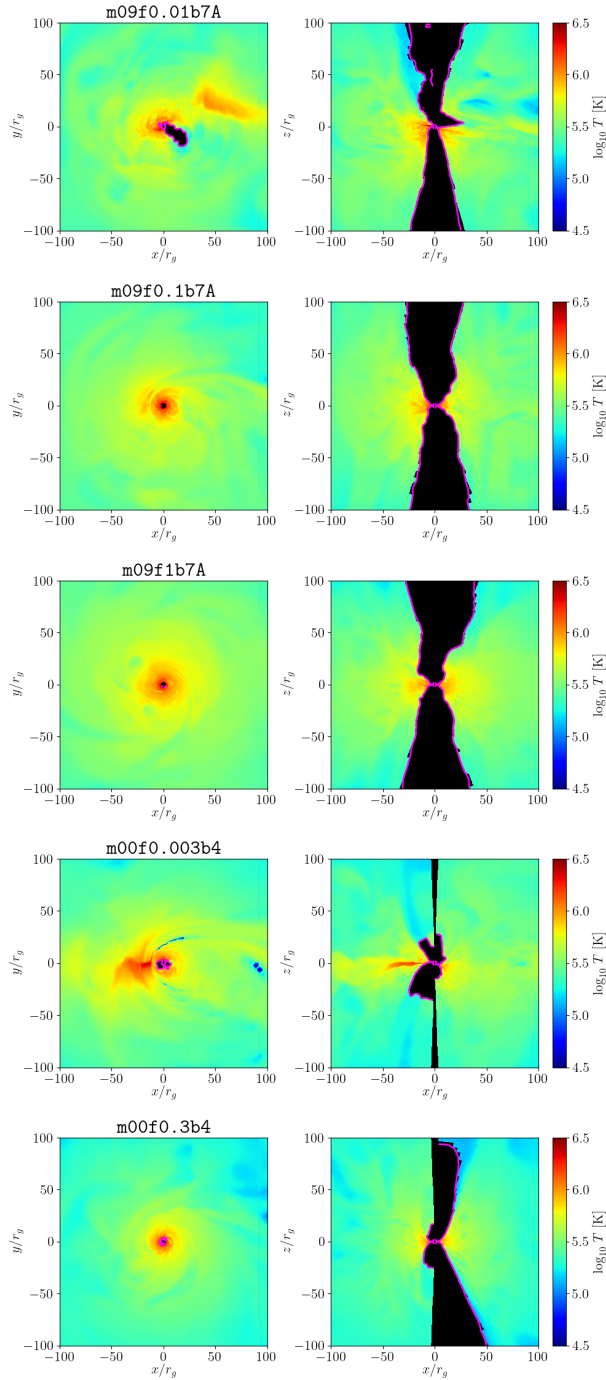


Figure 18. Here we show the gas temperature (colors) and $\sigma = 1$ boundary (pink line) for each model at the final snapshot. We mask the gas temperature in regions where $\sigma > 1$ for numerical reasons.

thick. We split the temperature into gas and radiation by solving

$$p_g = \frac{\rho k T}{\bar{m}} + \frac{1}{3} a T^4, \quad (43)$$

where \bar{m} is the mass per particle and T is the temperature. The gas temperature in the $\sigma > 1$ region is uncertain due to both numerical floors and the use of entropy inversion when energy conserving inversion fails in highly magnetized zones in GRMHD. As a result, we mask the gas temperature in

the jet/corona, but we generally expect it to be substantially hotter than the disk (Curd & Narayan 2019). We show the gas temperature for each model at $t = t_{\text{end}}$ in Figure 18.

In the accretion disk, since the gas and radiation pressure are split evenly, the gas temperature of the accretion disk reaches $T \sim 10^{5-6}$ K, which approximately agrees with Curd & Narayan (2019). Nozzle and self-intersection shocks also contribute to heating the gas and drive the temperature up to $\sim 10^6$ K at radii up to $50 - 100 r_g$.

In models with a prominent jet, the gas temperature may

exceed 10^6 K where $\sigma > 1$, which is in the range for X-ray photon production (Curd & Narayan 2019). Since the jet is able to prevent polar inflows, the poles will remain optically thin even at the peak of the fallback rate, allowing jet emission to emerge. Comptonization within this region is expected to produce a hard spectrum which shines even in the γ -ray band.

The non-jetted models on the other hand may have their X-ray emission largely absorbed if the photosphere is roughly spherical early on. Only after the funnel can form (or the photosphere recedes) can X-rays emerge.

6 DISCUSSION

6.1 Variability Driven by Violent Self-Intersection

*Swift*J1644+57 showed variability on a range of timescales with both short period QPOs at ~ 200 s (Reis et al. 2012) and long period dips in the light curve on time scales of $\sim 10^6$ s (Saxton et al. 2012). The short period QPOs are thought to originate from short term variability on the horizon scale due to orbits or resonances in the inner accretion disk. The long period variability has been suggested to arise from wobbling of the jet (Tchekhovskoy et al. 2014), periodic violent stream self-intersection (Andalman et al. 2022), or magnetic flux eruption events (Curd & Narayan 2023).

Previous global simulations of forming TDE disks have identified complete disruptions of the incoming stream in cases where $\beta = 3 - 7$ (Curd 2021; Andalman et al. 2022). The disruptions are temporally spaced by roughly the orbital period at the self-intersection radius. The fact that such a periodic dynamical effect took place was viewed as an attractive explanation for the variability in J1644+57. However, with no magnetic fields or radiative transfer calculations available, Andalman et al. (2022) hypothesized that this interaction could drive flaring through changes in the mass accretion rate at the horizon.

As shown in Section 5.5, we directly relate the complete disruptions during self-intersection with jet variability. Since the total efficiency in Figure 16 correlates directly to jet power in MAD accretion disks, this can account for the large drops in the flux seen in J1644+57, which had minima as low as $\lesssim 50\%$ of the maximum. This is solid confirmation of the idea proposed by Andalman et al. (2022); however, we suggest that flaring is not because of changes in the mass accretion rate directly. Rather, it is the fact that the stream acts to keep magnetic flux anchored to the BH. The magnetic flux threading the BH is at the saturation value prior to the stream disrupts itself during self-intersection. When the feeding from incoming steam material is temporarily halted, magnetic flux eruptions shed flux until ϕ_{BH} settles to a lower value. The disk injection simulations presented in Curd & Narayan (2023) found that after flux eruption events the magnetic flux took roughly the orbital period at the injection radius to recover. This is dynamically similar to the effects seen in this work; however, here the period is directly related to the self-intersection radius rather than the gas injection radius.

Given the relationship between the variability period and the self-intersection radius, this suggests that X-ray variability can be related to the orbital properties of the disrupted

star in a jetted TDE. For instance, assuming $M_{\text{BH}} = 10^6 M_{\odot}$ for J1644+57, the roughly 10^6 second variability corresponds to a self-intersection radius on the order of $10^3 r_g$. For an $a_* = 0$ BH, this corresponds to a $\beta \sim 1.5$ TDE. The steady increase in the variability period may be due to an increase in the self-intersection radius as the disk builds up over time as illustrated by Ryu et al. (2023).

We will explore the properties of magnetized TDE disks and magnetic flux saturation in more detail in a future report.

6.2 Could Disk Collapse Still Be Dynamically Important in a MAD?

Simulations of thin MADs presently negate the idea that TDEs will rapidly shed magnetic flux and resemble a standard thin disk as the accretion rate goes below Eddington. The powerful fields in a MAD provide support against runaway thermal collapse. This may only apply to the inner disk. Here we treat the thermal instability of the entire disk and examine how changes in f_{ρ} may lead to tilt evolution of the disk/jet without it becoming non-MAD.

Since the mass fallback rate in TDEs evolves from super- to sub-Eddington, it is thought that the mass accretion rate in the disk will evolve similarly assuming $\dot{M} \sim \dot{M}_{\text{fb}}$. We can apply standard accretion theory to predict the geometry of the accretion disk over time.

In an accretion disk, angular momentum transport is driven by viscosity and this drives accretion onto the BH but also heats the disk (See Abramowicz et al. 1988; Abramowicz & Fragile 2013 for an introductory discussion). In order for the disk to remain stable, it cools through advection and radiation. In super-Eddington disks, the disk is optically thick and cooling is dominated by advective cooling, Q_{adv}^- . Dynamically, this means radiation within the disk is advected with the inflow and eventually crosses the BH horizon. In thin disks, energy generated by viscous heating is radiated locally and cooling is dominated by radiation, Q_{rad}^- . Since radiation pressure dominates in super-Eddington systems, the accretion disk puffs up to a large scale-height $h_d \equiv H_d/R \gtrsim 0.3$ when radiation cannot escape directly, or $Q_{\text{adv}}^- \gg Q_{\text{rad}}^-$.

If the system is in a steady state, meaning that the mass accretion rate is constant with radius, advective and radiative cooling vary with radius. We assert that a steady state is a reasonable assumption even in the chaotic environment of a TDE since \dot{M} was found to be roughly constant with radius in Curd (2021). Following Sadowski (2011), we can write the ratio between advective and radiative cooling

$$\frac{Q_{\text{adv}}^-}{Q_{\text{rad}}^-} \approx \dot{M} \frac{\kappa_{\text{es}} h_d}{\pi R c}, \quad (44)$$

where h_d is the disk scale-height and κ_{es} is the electron scattering opacity. From this expression, it is clear that as the accretion rate declines radiative cooling begins to become more significant until a critical accretion rate (which is around Eddington) where it becomes dominant. Assuming \dot{M} and h_d are constant and setting $\kappa_{\text{es}} = 0.2(1 + X)\text{cm}^2 \text{g}^{-1}$ where $X = X_{\odot} = 0.7381$ is the solar hydrogen mass fraction, we can approximate the transition radius where advective and radiative cooling terms balance (or $Q_{\text{adv}}^- = Q_{\text{rad}}^-$)

$$R_{\text{tr}} = \dot{M} \frac{\kappa_{\text{es}} h_d}{\pi c}. \quad (45)$$

From the above expression, we can conclude that (i) R_{tr} scales linearly with mass accretion rate and thus shrinks over time in a TDE, (ii) we expect the system to become thermally unstable at $r > R_{\text{tr}}$. Assuming the disk is heated purely by viscosity, collapse occurs on the thermal timescale $t_{\text{th}} \sim (\alpha\Omega)^{-1}$, where Ω is the angular velocity and α is the unitless viscosity parameter. We note that we have ignored other sources of heating such as dissipative heating due to the shocks for simplicity in our calculation of R_{tr} . If heating generated by shocks is not radiated locally, regions of the disk which have become thermally unstable by the condition $Q_{\text{adv}}^- < Q_{\text{rad}}^-$ may remain stable and geometrically thick.

The first shock we consider is the self-intersection shock which can release a large amount of energy, especially for relativistic TDEs. We account for heating by the self-intersection shock by first approximating the self-intersection radius. We adopt a similar method to Dai et al. (2015) to quantify apsidal precession. For material making its first pericenter passage, the precession angle may be approximated by

$$\Delta\phi = \frac{6\pi}{a(1-e^2)}. \quad (46)$$

Here e is the eccentricity of the incoming stream and a is the semi-major axis. Note that we have expressed $\Delta\phi$ using gravitational units so the semi-major axis a is given in gravitational radii. Treating the orbits of the incoming stream that has yet to pass through pericenter and the already precessed stream as ellipses, the self-intersection between the incoming material and material that has precessed occurs at the radius

$$R_{\text{SI}} = \frac{(1+e)R_t}{\beta(1-e\cos(\Delta\phi/2))}. \quad (47)$$

The self-intersection shock releases energy at a rate of roughly

$$L_{\text{SI}}(t) \approx \frac{1}{2} \dot{M}_{\text{fb}}(t) v_{\text{SI}}^2, \quad (48)$$

where the velocity at which the streams collide, v_{SI} , is on the order of the free-fall velocity. As the velocity of the stream elements is greater at smaller radii, the rate of dissipation will also be greater for closer orbits. We note that our definition of R_{SI} assumes $a_{\text{BH}} = 0$; however, $a_{\text{BH}} > 0$ BHs can cause smaller R_{SI} at lower β for retrograde TDEs due to frame dragging effects.

Shocks are present in the disk throughout the evolution and are also sites of dissipative heating (Shiokawa et al. 2015; Sadowski et al. 2016; Liptai et al. 2019; Ryu et al. 2023). The $\beta = 1$ model in Liptai et al. (2019) showed dissipation from shocks exceed Eddington at up to ten times t_{fb} . Ryu et al. (2023) estimate the total mechanical energy output and find that it exceeds Eddington even after $2t_{\text{fb}}$, though they do not isolate energy from shocks. Since the spiral shocks are spread over the majority of the disk, energy generated from the shocks is expected to not be localized.

Energy released from shocks may delay thermal collapse assuming it is instantaneously spread evenly in the disk. If the disk radiates at L_{Edd} , elements of the outer disk which are already thermally unstable by the condition $Q_{\text{adv}}^- < Q_{\text{rad}}^-$ cannot collapse until the dissipation rate from shocks is less than Eddington. We define the time when the dissipation rate from shocks is less than L_{Edd} as t_{Edd} . To illustrate how thermal collapse occurs, it is instructive to compute the time

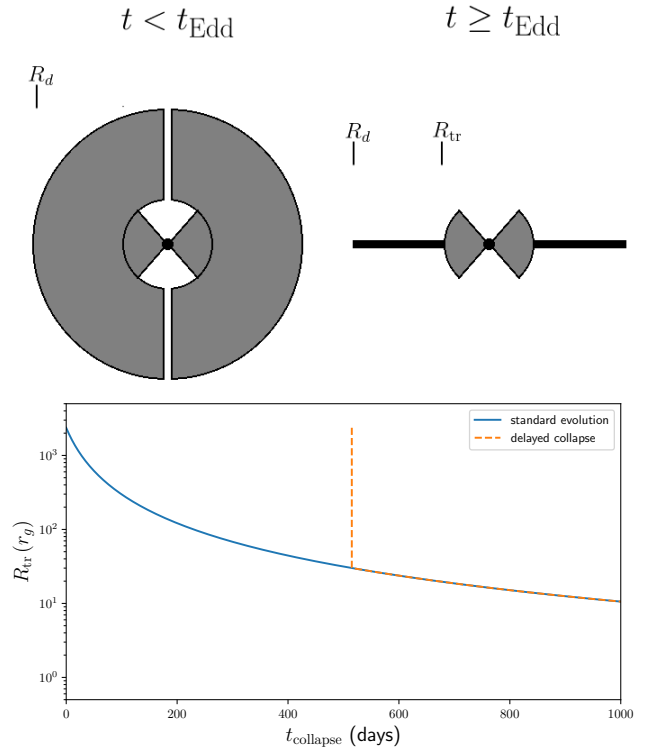


Figure 19. In the top panel, we illustrate a delayed disk collapse model where the accretion disk remains geometrically thick all the way to the transition radius (R_{tr}) until $t \geq t_{\text{Edd}}$. In the bottom panel, we show the collapse time (t_{collapse}) as a function of radius in the disk for a $m_6 = 1$, $m_* = 1$, and $\beta = 1$ TDE with (dashed line) and without (solid line) delayed thermal collapse. In our delayed collapse model, larger radii are prevented from cooling early on and a large portion of the disk has the same collapse time (vertical portion of dashed line).

at which the disk component at R_{tr} will collapse,

$$t_{\text{collapse}} = \begin{cases} t + t_{\text{th}}, & t \geq t_{\text{Edd}} \\ t_{\text{Edd}}, & t < t_{\text{Edd}}, \end{cases} \quad (49)$$

where t is the time since the initial disruption.

We show examples of t_{collapse} versus R_{tr} in Figure 19 for $m_6 = 1$, $m_* = 1$, and $\beta = 1$ TDE. We assume a Keplerian profile in both models (since the disk is circularized) and $\alpha = 0.1$ such that $t_{\text{th}} \propto R^{3/2}$. In a standard accretion disk, the outer disk will collapse first and R_{tr} slowly decreases over several hundred days. As a result, the ram pressure acting on the stream will also slowly increase since the bulk of the disk will still be geometrically thick until $R_{\text{tr}} \sim r_H$. Thus, a model where the transition radius depends only on mass accretion cannot explain rapid state transitions since $R_{\text{tr}} \propto \dot{M} \propto t^{-5/3}$. For the collapsing disk model, we assume $t_{\text{Edd}} = 515$ days to be similar to *Swift* J1644+57. Since the energy injected into the disk is assumed to exceed the radiated energy of the system until $t > t_{\text{Edd}}$, the outer disk will remain geometrically thick until it collapses (the vertical part of the curve in Figure 19) on the thermal time scale which is much smaller than t . Once $t > t_{\text{Edd}}$, the inner disk follows the standard accretion curve. Here we have ignored the possibility of magnetic pressure support for simplicity.

For an assumed state transition at several hundred days,

only the delayed collapse model will have an instantaneous change in f_ρ over most of the disk. This will lead to the desired dynamical consequences on the jet and disk. That is, the density contrast of the collapsed region of the disk will rapidly increase by more than an order of magnitude at t_{collapse} since the disk density in Equation 9 for $r > R_{\text{tr}}$ will be multiplied by a factor of h_d^{-1} . This will lead to the self-intersection outflow rapidly ceasing as in our simulations, in which case the disk and jet will rapidly realign with the BH spin due to the disk being MAD. We also note the possibility of radial contraction of the disk (or a decrease in R_d) as in Metzger (2022) would only enhance the rise in f_ρ . As such, we expect that the effects of disk collapse will play a role dynamically; however, our analysis favors relativistic TDEs with $\beta > 1$ (or retrograde TDEs) if self-intersection is the assumed method of delaying disk collapse.

6.3 Tilt Evolution in Jetted TDEs

Our simulations illustrate that even an aligned TDE can undergo strong tilt excitation when a jet is present. The fact that the tilt decreases when the density contrast increases, which is due to the self-intersection shock and outflow being weakened, suggests that X-ray shut-off in TDE jets may be possible even without the disk exiting the MAD state.

We produce a toy model of a relativistic jet where the tilt and flux depend on f_ρ . The tilt is assumed to be

$$\mathcal{T}_{\text{jet}}(f_\rho) = \mathcal{T}_{\text{jet},0} \begin{cases} 1, & f_\rho < f_{\rho,\text{min}} \\ \left(1 - \frac{f_\rho - f_{\rho,\text{min}}}{f_{\rho,\text{max}} - f_{\rho,\text{min}}}\right), & f_{\rho,\text{min}} \leq f_\rho \leq f_{\rho,\text{max}} \\ 0, & f_\rho > f_{\rho,\text{max}}. \end{cases} \quad (50)$$

Here we have assumed that the jet angle is constant when the stream is dense enough for the self-intersection shock to occur. It then linearly decreases from $\mathcal{T}_{\text{jet},0}$ to 0 as f_ρ increases from $f_{\rho,\text{min}}$ to $f_{\rho,\text{max}}$. Here $f_{\rho,\text{min}}$ is the critical density contrast where self-intersection is weak enough for the jet to begin to realign and $f_{\rho,\text{max}}$ is where the jet is completely unperturbed.

The X-ray variability in *Swift* J1644+57 indicates that X-rays originate from near the BH, so we use a simple top-hat jet model and incorporate beaming effects to predict the time evolution of the flux. We adopt a model similar to Beniamini et al. (2023) where the off-axis jet flux is proportional to the on-axis jet flux through a simple beaming correction factor

$$a = \frac{1 - \beta_{\text{jet}}}{1 - \beta_{\text{jet}} \cos(\mathcal{T}_{\text{obs}} - \mathcal{T}_{\text{jet}})} \quad (51)$$

is the beaming correction, where β_{jet} is the jet velocity \mathcal{T}_{obs} is the angle of the observer relative to the z -axis. The flux is approximated as

$$F(\mathcal{T}_{\text{jet}}) = F_{\text{on,jet}}(t) \begin{cases} 1, & \Delta\theta < \theta_{\text{jet}} \\ 0.5a^2, & \theta_{\text{jet}} < \Delta\theta < 2\theta_{\text{jet}} \\ 0.5a^3, & \Delta\theta > 2\theta_{\text{jet}}. \end{cases} \quad (52)$$

Here $\Delta\theta \equiv \mathcal{T}_{\text{obs}} - \mathcal{T}_{\text{jet}}$ and $\theta_{\text{jet}} = \gamma_{\text{jet}}^{-1}$ is the angle that the jet is beamed into. The factor of 0.5 is a geometrical correction. We assume that the jet flux is directly correlated to the mass accretion rate, which we assume to be a fraction of

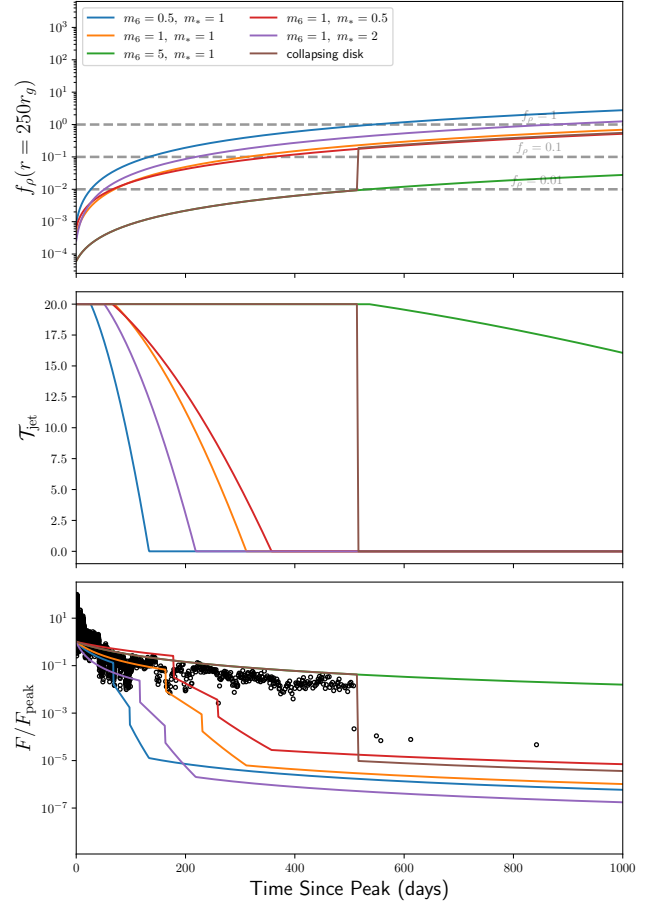


Figure 20. In the top panel, we illustrate how f_ρ evolves in our simple disk model described in Section 2 with a range of BH mass $m_6 = M_{\text{BH}}/10^6 M_\odot$ and stellar mass $m_* = M_*/M_\odot$. Note that we set $f_{\text{acc}} = 0.1$ in each profile for simplicity. We show the initial f_ρ for each simulation with $a_* = 0.9$ models in Table 1 based on M_{inj} (horizontal dashed lines). We also show a case where we assume disk collapse at $t = t_{\text{Edd}}$ for $m_6 = 5$ and $m_* = 1$ (brown line). In the middle panel, we show the jet tilt from Equation 50 assuming $\mathcal{T}_{\text{jet},0} = 20^\circ$, $f_{\rho,\text{min}} = 0.01$, and $f_{\rho,\text{max}} = 0.1$. In the bottom panel, we show the beamed jet flux computed from Equation 52 assuming $\mathcal{T}_{\text{obs}} = \mathcal{T}_{\text{jet},0}$. We compare each model with the normalized X-ray flux from *Swift* J1644+57 taken from Zauderer et al. (2013); Eftekhari et al. (2018); Cendes et al. (2021) (black circles). Models without collapse show a steady decrease in jet flux as the jet angle changes. Only the model which assumes disk collapse reasonably explains the > 2 order of magnitude decrease in X-ray flux observed in *Swift* J1644+57.

the fallback rate $F_{\text{on,jet}}(t) \propto \dot{M}_{\text{fb}}(t)$. We divide the flux by $F_{\text{on,jet}}(t=0) = F_{\text{peak}}$ for simplicity.

We apply our toy model to a range of TDEs in Figure 20. For the disk/stream interaction, we set $f_{\rho,\text{min}} = 0.01$ and $f_{\rho,\text{max}} = 0.1$. For the jet, we assume $\gamma_{\text{jet}} = 10$, $\mathcal{T}_{\text{jet},0} = 20^\circ$. The observer is assumed to be aligned with the jet initially with $\mathcal{T}_{\text{obs},0} = 20^\circ$. In addition to smoothly varying f_ρ models, we also analyse a collapsing disk model, motivated by the discussion in Section 6.2, with $m_6 = 5$, $m_* = 1$, $\beta = 1$ which instantaneously collapses to $h_d = 0.05$ at $t = t_{\text{Edd}} = 515$ days.

Our model illustrates that if the band of f_ρ where the self-

intersection weakens is large, the jet cannot shift by tens of degrees in 1-2 weeks. A rapid shutoff may instead be related to the collapse of the outer disk which causes a rapid spike in f_ρ and a subsequent rapid realignment of the jet, as illustrated by the 'collapsing disk' model. Due to relativistic beaming, this can account for the more than 2 orders of magnitude drop in X-rays at ~ 500 days in less than 15 days jetted TDEs like *Swift* J1644+57 with the appropriate TDE parameters.

Note that we only require that the X-ray emission decrease by at least two orders of magnitude within ~ 2 weeks in order to explain the behaviour of *Swift* J1644+57. The X-rays after the decline could be disk emission which becomes dominant when the jet is out of the line of sight. This is more attractive of an explanation since the jet emission follows a $t^{-5/3}$ power law even after tilting, but the late time X-rays are approximately constant.

6.4 Coronal Evolution in Non-Jetted TDEs

Tilt effects are unlikely to lead to substantial X-ray changes in non-jetted TDEs since the emitting region is non-relativistic and we only saw changes of up to $\sim 10^\circ$ in our models. However, our $a_* = 0$ simulations demonstrate that a coronal region can be sustained even during stream self-intersection provided enough magnetic flux threads the disk/BH. Curd (2021) found no funnel/corona region during the stream injection phase due to a substantially lower magnetic flux than our MAD disks, but this may only apply to the TDE evolution near the peak fallback rate as their simulations covered only a few days of evolution. Assuming magnetic flux increases as a function of time, which appears to occur in TDE disks (Sadowski et al. 2016), our $a_* = 0$ simulations may be interpreted as the limiting state for a TDE at a given f_ρ around a Schwarzschild BH since they are MAD. Increases in X-ray emission in non-jetted TDEs may then be related to both a hot, magnetized corona forming as ϕ increases combined with a decrease in optical depth as the fall back rate declines. The X-rays during this phase would exhibit a slow rise as the photosphere radius drops.

The X-ray emission in AT2021ehb steadily turned on until it reached a maximum of $\sim 5 \times 10^{43} \text{ erg s}^{-1}$ before promptly declining by an order of magnitude at ~ 270 days. The rise phase and spectral hardening of AT2021ehb could be explained by the coronal evolution scenario outlined in the previous paragraph while the rapid decrease in X-ray flux could conceivably be due to the delayed disk collapse we discuss in Section 6.2. While the coronal evolution in our non-jetted models is expected to be similar to a non-MAD case, whether or not thermal TDEs are also MAD is unclear and simulations which evolve the magnetic field suggest they should not be. This leads to important dynamical differences when considering the evolution of the disk. While a MAD disk may remain magnetic pressure supported, non-MAD accretion disks are expected to become thermally unstable once pressure support from shocks is lost.

6.5 Future Prospects

The discovery of tilt instability in TDE disks could have profound consequences on the emission properties beyond the

X-ray emission from the jet or corona. It is conceivable that the polarization signal of the disk and jet will be impacted by changes in the tilt of the system.

Although we found some evidence of enhanced magnetic flux accumulation in model m09f0.01b7, the turbulent dynamics near the horizon may have impeded this effect. The onset of the disk tilt also seems to correspond with a decrease of the magnetic flux at the horizon. Simulations with the self intersection radius move further away from the horizon may allow higher magnetic flux to be sustained. This may lead to a magnetic flux much higher than expected by Tchekhovskoy et al. (2014).

Curd et al. (2022, 2023) investigated the morphology and radio spectra of jets from SANE super-Eddington accretion disks. Such an analysis could similarly be carried out on MAD TDE disks and would provide useful insight into how the dynamics of the system effect the ultimate jet properties. We plan to investigate this in a future work.

7 CONCLUSIONS

- All of our simulations maintained a significant magnetic flux threading the horizon even after interacting with the TDE stream. Each simulation reached a MAD or semi-MAD state. Powerful jets were launched for $a_* = 0.9$ models. This is strong validation of the idea that TDEs can become MAD and launch spin-powered jets.

- We found that the Maxwell stress is subdominant to hydrodynamic sources of viscosity at all values of f_ρ investigated in this work. Instead, shocks and hydrodynamic viscosity drive angular momentum transport.

- The strength of the self-intersection outflow depends on the ratio between the stream and the disk. As the stream becomes less dense, ram pressure from the disk can effectively brake the stream and it eventually joins with the disk with either a weak self-intersection or no self-intersection at all.

- During the early stages of a TDE, the stream is much denser than the disk with $f_\rho < 0.01$ since most of the mass has yet to fallback. The stream is essentially unperturbed by the disk at this stage and has a strong self-intersection shock since it maintains its orbital energy. The self-intersection outflow pushes on the jet/corona region. This tilts the jet/corona by $10 - 40^\circ$ in our simulations. As f_ρ increases, the self-intersection shock weakens and powerful jets remain aligned with the BH spin.

- In jetted TDEs, because the jet is tilted by the self-intersection outflow, the jet can transfer momentum to the disk, which tilts the disk to $\sim 20 - 30^\circ$ in less than $10,000 t_g$. This configuration is stable due to the self-intersection of tilted material within R_{SI} with un-tilted material being brought in from the stream. This effect does not occur when there is no self-intersection outflow (the stream is not dense enough) or there is no jet (as shown by our $a_* = 0$ models).

- When we lowered the stream density in a restart of the model m09f0.01b7 after the disk/jet was tilted, we found that a MAD or semi-MAD state leads to alignment of the disk/jet similar to GRMHD simulations of tilted disks. We propose that this is due to the weakening/absence of the self-intersection, which acts to maintain the tilt once it sets in.

- We demonstrate that rapid changes in f_ρ , which may occur due to delayed disk collapse, will lead to a rapid X-ray

shutoff in jetted TDEs. Jet realignment with the BH spin in models m09f1b7B and m09f0.1b7B represents a change of $\sim 20 - 30^\circ$ in the jet angle in less than three days. We propose that this is an alternative method of rapidly dropping the X-ray flux in *Swift* J1644+57 in ~ 15 days without also requiring that the system no longer be MAD.

8 ACKNOWLEDGEMENTS

We thank Enrico Ramirez-Ruiz for useful suggestions during preparation of the manuscript. We thank Aviyel Ahiyya for assistance with obtaining observational data. This work was supported by the Simons Collaboration on Extreme Electrodynamics of Compact Sources. Richard Jude Anantua was supported by the Oak Ridge Associated Universities Powe Award for Junior Faculty Enhancement. Computational support was provided via ACCESS resources (grant PHY230006).

9 DATA AVAILABILITY

The data underlying this article will be shared on reasonable request to the corresponding author.

REFERENCES

- Abramowicz M. A., Fragile P. C., 2013, *Living Reviews in Relativity*, **16**, 1
- Abramowicz M. A., Czerny B., Lasota J. P., Szuszkiewicz E., 1988, *ApJ*, **332**, 646
- Alexander K. D., Berger E., Guillochon J., Zauderer B. A., Williams P. K. G., 2016, *ApJ*, **819**, L25
- Alexander K. D., Wieringa M. H., Berger E., Saxton R. D., Komossa S., 2017, *ApJ*, **837**, 153
- Alexander K. D., van Velzen S., Horesh A., Zauderer B. A., 2020, *Space Sci. Rev.*, **216**, 81
- Andalman Z. L., Liska M. T. P., Tchekhovskoy A., Coughlin E. R., Stone N., 2022, *MNRAS*, **510**, 1627
- Avara M. J., McKinney J. C., Reynolds C. S., 2016, *MNRAS*, **462**, 636
- Beniamini P., Piran T., Matsumoto T., 2023, *MNRAS*, **524**, 1386
- Bloom J. S., et al., 2011, *Science*, **333**, 203
- Bonnerot C., Lu W., 2020, *MNRAS*, **495**, 1374
- Bonnerot C., Rossi E. M., Lodato G., Price D. J., 2016, *MNRAS*, **455**, 2253
- Bonnerot C., Lu W., Hopkins P. F., 2021, *MNRAS*, **504**, 4885
- Brassart M., Luminet J. P., 2010, *A&A*, **511**, A80
- Bricman K., Gomboc A., 2020, *ApJ*, **890**, 73
- Brown G. C., Levan A. J., Stanway E. R., Tanvir N. R., Cenko S. B., Berger E., Chornock R., Cucchiara A., 2015, *MNRAS*, **452**, 4297
- Burrows D. N., et al., 2011, *Nature*, **476**, 421
- Carter B., Luminet J. P., 1982, *Nature*, **296**, 211
- Cendes Y., Eftekhari T., Berger E., Polisensky E., 2021, *ApJ*, **908**, 125
- Cenko S. B., et al., 2012, *ApJ*, **753**, 77
- Chan C.-H., Piran T., Krolik J. H., Saban D., 2019, *ApJ*, **881**, 113
- Chatterjee K., Narayan R., 2022, *ApJ*, **941**, 30
- Chatterjee K., Liska M., Tchekhovskoy A., Markoff S. B., 2019, *MNRAS*, **490**, 2200
- Coughlin E. R., Begelman M. C., 2014, *ApJ*, **781**, 82
- Coughlin E. R., Nixon C., 2015, *ApJ*, **808**, L11
- Coughlin E. R., Nixon C., Begelman M. C., Armitage P. J., 2016, *MNRAS*, **459**, 3089
- Curd B., 2021, *MNRAS*, **507**, 3207
- Curd B., Narayan R., 2019, *MNRAS*, **483**, 565
- Curd B., Narayan R., 2023, *MNRAS*, **518**, 3441
- Curd B., Emami R., Roelofs F., Anantua R., 2022, *Galaxies*, **10**, 117
- Curd B., Emami R., Anantua R., Palumbo D., Doeleman S., Narayan R., 2023, *MNRAS*, **519**, 2812
- Dai L., McKinney J. C., Miller M. C., 2015, *ApJ*, **812**, L39
- Dai L., McKinney J. C., Roth N., Ramirez-Ruiz E., Miller M. C., 2018, *ApJ*, **859**, L20
- Eftekhari T., Berger E., Zauderer B. A., Margutti R., Alexander K. D., 2018, *ApJ*, **854**, 86
- Evans C. R., Kochanek C. S., 1989, *ApJ*, **346**, L13
- Gammie C. F., McKinney J. C., Tóth G., 2003, *ApJ*, **589**, 444
- Gezari S., 2021, *ARA&A*, **59**, 21
- Golightly E. C. A., Nixon C. J., Coughlin E. R., 2019, *ApJ*, **882**, L26
- Guillochon J., Ramirez-Ruiz E., 2013, *ApJ*, **767**, 25
- Hammerstein E., et al., 2023, *ApJ*, **942**, 9
- Hayasaki K., Stone N., Loeb A., 2016, *MNRAS*, **461**, 3760
- Hills J. G., 1975, *Nature*, **254**, 295
- Hinkle J. T., et al., 2021, *MNRAS*, **500**, 1673
- Holoien T. W. S., et al., 2019, *ApJ*, **883**, 111
- Holoien T. W. S., et al., 2020, *ApJ*, **898**, 161
- Ivezić Ž., et al., 2019, *ApJ*, **873**, 111
- Jiang Y.-F., Guillochon J., Loeb A., 2016, *ApJ*, **830**, 125
- Kato Y., Mineshige S., Shibata K., 2004, *ApJ*, **605**, 307
- Kelley L. Z., Tchekhovskoy A., Narayan R., 2014, *MNRAS*, **445**, 3919
- Kochanek C. S., 1994, *ApJ*, **422**, 508
- Komossa S., 2015, *Journal of High Energy Astrophysics*, **7**, 148
- Liptai D., Price D. J., Mandel I., Lodato G., 2019, *arXiv e-prints*, p. arXiv:1910.10154
- Liska M., Tchekhovskoy A., Quataert E., 2020, *MNRAS*, **494**, 3656
- Liska M. T. P., Musoke G., Tchekhovskoy A., Porth O., Beloborodov A. M., 2022, *ApJ*, **935**, L1
- Lodato G., King A. R., Pringle J. E., 2009, *MNRAS*, **392**, 332
- Mainetti D., Lupi A., Campana S., Colpi M., Coughlin E. R., Guillochon J., Ramirez-Ruiz E., 2017, *A&A*, **600**, A124
- McKinney J. C., Tchekhovskoy A., Blandford R. D., 2012, *MNRAS*, **423**, 3083
- Metzger B. D., 2022, *ApJ*, **937**, L12
- Metzger B. D., Stone N. C., 2016, *MNRAS*, **461**, 948
- Narayan R., Yi I., 1995, *ApJ*, **452**, 710
- Narayan R., Igumenshchev I. V., Abramowicz M. A., 2003, *PASJ*, **55**, L69
- Narayan R., Chael A., Chatterjee K., Ricarte A., Curd B., 2022, *MNRAS*, **511**, 3795
- Novikov I. D., Thorne K. S., 1973, in *Black Holes (Les Astres Occlus)*. pp 343–450
- Paczynsky B., Wiita P. J., 1980, *A&A*, **88**, 23
- Pasham D. R., et al., 2015, *ApJ*, **805**, 68
- Phinney E. S., 1989, in Morris M., ed., Vol. 136, *The Center of the Galaxy*. p. 543
- Ramirez-Ruiz E., Rosswog S., 2009, *ApJ*, **697**, L77
- Rees M. J., 1988, *Nature*, **333**, 523
- Reis R. C., Miller J. M., Reynolds M. T., Gültekin K., Maitra D., King A. L., Strohmayer T. E., 2012, *Science*, **337**, 949
- Ressler S. M., White C. J., Quataert E., Stone J. M., 2020, *ApJ*, **896**, L6
- Ryu T., Krolik J., Piran T., Noble S. C., 2020, *ApJ*, **904**, 99
- Ryu T., Krolik J., Piran T., Noble S., Avara M., 2023, *arXiv e-prints*, p. arXiv:2305.05333
- Sadowski A., 2011, *arXiv e-prints*, p. arXiv:1108.0396
- Sadowski A., Tejeda E., Gafton E., Rosswog S., Abarca D., 2016, *MNRAS*, **458**, 4250

- Saxton C. J., Soria R., Wu K., Kuin N. P. M., 2012, *MNRAS*, **422**, 1625
- Shiokawa H., Krolik J. H., Cheng R. M., Piran T., Noble S. C., 2015, *ApJ*, **804**, 85
- Śądowski A., Narayan R., 2015, *MNRAS*, **453**, 3213
- Śądowski A., Narayan R., Penna R., Zhu Y., 2013, *MNRAS*, **436**, 3856
- Śądowski A., Narayan R., McKinney J. C., Tchekhovskoy A., 2014, *MNRAS*, **439**, 503
- Śądowski A., Narayan R., Tchekhovskoy A., Abarca D., Zhu Y., McKinney J. C., 2015, *MNRAS*, **447**, 49
- Steinberg E., Stone N. C., 2022, *arXiv e-prints*, p. arXiv:2206.10641
- Steinberg E., Coughlin E. R., Stone N. C., Metzger B. D., 2019, *MNRAS*, **485**, L146
- Stone N., Sari R., Loeb A., 2013, *MNRAS*, **435**, 1809
- Strubbe L. E., Quataert E., 2009, *MNRAS*, **400**, 2070
- Tchekhovskoy A., Narayan R., McKinney J. C., 2011, *MNRAS*, **418**, L79
- Tchekhovskoy A., McKinney J. C., Narayan R., 2012, in *Journal of Physics Conference Series*. p. 012040 (arXiv:1202.2864), doi:10.1088/1742-6596/372/1/012040
- Tchekhovskoy A., Metzger B. D., Giannios D., Kelley L. Z., 2014, *MNRAS*, **437**, 2744
- Teboul O., Metzger B. D., 2023, *arXiv e-prints*, p. arXiv:2308.05161
- Zauderer B. A., et al., 2011, *Nature*, **476**, 425
- Zauderer B. A., Berger E., Margutti R., Pooley G. G., Sari R., Soderberg A. M., Brunthaler A., Bietenholz M. F., 2013, *ApJ*, **767**, 152

APPENDIX A: ADDITIONAL GRID DETAILS

We adapt modified Kerr-Schild coordinates with the inner radius of the simulation domain inside of the BH horizon. The uniformly spaced internal coordinates (x_1, x_2, x_3) are related to the Kerr-Schild spherical polar coordinates polar coordinates (r, ϑ, φ) by

$$r = e^{x_1}, \quad (\text{A1})$$

$$\vartheta = \left[1 + \cot \left(\frac{H_0 \pi}{2} \right) f_{\vartheta}(x_1) \right] \frac{\pi}{2}, \quad (\text{A2})$$

$$\varphi = x_3. \quad (\text{A3})$$

The function in the middle expression is

$$f_{\vartheta}(x_1) = \tan \left(H_0 \pi \left[-0.5 + \left(Y_1 + \frac{(-Y_1 + Y_2)}{(e^{x_1}/2)^{P_0}} \right) (1 - 2x_2) + x_2 \right] \right). \quad (\text{A4})$$

The expression for ϑ is designed such that (i) the minimum/maximum coordinate ϑ is radially dependent, and (ii) more cells are focused towards the midplane $\vartheta = \pi/2$. We choose $H_0 = 0.7$ to add slightly more resolution in the midplane in order to better resolve the accretion disk. We also choose $Y_1 = 0.001$, $Y_2 = 0.02$, and $P_0 = 1.5$ such that $Y_2 \pi < \vartheta < (1 - Y_2) \pi$ near the horizon but $Y_1 \pi < \vartheta < (1 - Y_1) \pi$ further away. This choice ultimately increases the minimum time step and decreases the computational cost of each simulation.

APPENDIX B: INITIAL CONDITIONS

We use the power law angular momentum disk in hydrostatic equilibrium that was presented in Kato et al. (2004) to initialize the torus in the KORAL code.

For the model presented in Kato et al. (2004), they use the pseudo-Newtonian potential described in Paczyński & Wiita (1980):

$$\phi = -\frac{GM}{(R - R_S)}, \quad (\text{B1})$$

where R is the radius in polar coordinates, and R_S is the Schwarzschild radius. A polytropic equation of state is assumed such that $p = K\rho^{1+1/n}$ and the angular momentum distribution of the disk is assumed to be a power law given by:

$$l(r, z) = l_0 \left(\frac{r}{r_0} \right)^a, \quad (\text{B2})$$

where r and z are the cylindrical radius and height, and $l_0 = (GMr_0^3)^{1/2}/(r_0 - R_S)$. Here r_0 is simply a scale radius that sets the pressure and density maximum and a is a constant. Under these assumptions, the condition for hydrostatic equilibrium combined with the polytropic equation of state yields a complete solution for the entire torus given the pressure (p_0) and density (ρ_0) at the characteristic radius r_0 :

$$\rho = \rho_0 \left[1 - \frac{\gamma}{v_{s,0}^2} \frac{(\psi - \psi_0)}{n + 1} \right]^n, \quad (\text{B3})$$

$$p = \rho_0 \frac{v_{s,0}^2}{\gamma} \left(\frac{\rho}{\rho_0} \right)^{1+1/n}, \quad (\text{B4})$$

where γ is the adiabatic index (which we set to $4/3$ since the torus is radiation dominated which implies $n = 3$), $v_s = \sqrt{\gamma p/\rho}$ is the sound speed of the gas, $\psi = \phi + \xi = -GM/(R - R_S) - l^2/2r^2(1 - a)$ is the effective potential. Here ξ is the centrifugal potential.

The Bernoulli parameter for the gas is given by the sum of the specific kinetic, potential, and internal energy. The gas is initially on a Keplerian orbit so the Bernoulli parameter is:

$$\text{Be} = (1 - a)\xi + \phi + \psi_{\text{int}}, \quad (\text{B5})$$

where $\psi_{\text{int}} = \gamma p/(\gamma - 1)\rho$ is the internal potential. The condition of hydrostatic equilibrium satisfies the equation $\nabla(\xi + \phi + \psi_{\text{int}}) = 0$, which implies:

$$\xi + \phi + \psi_{\text{int}} = \text{constant}. \quad (\text{B6})$$

Theoretical studies of TDE disks find that the gas comes in with roughly equal angular momentum. As such, we use a constant angular momentum model in this work. This implies that we should choose $a = 0$. Under this condition, the Bernoulli parameter of the disk is also constant given equations (B5) and (B6).

To initialize the disk within the KORAL code, we specify the characteristic radius (r_0), maximum density (ρ_0), and initial gas temperature at the density maximum (T_0). We set the characteristic radius $r_0 = 20r_g$. The initial gas density is $\rho_0 = 1.986 \times 10^{-8} \text{g cm}^{-3}$ to give an initial accretion rate roughly 10 times the Eddington mass accretion rate, and the gas temperature $T_0 = 3.5 \times 10^{10} \text{K}$ is chosen such that the initial torus extends to roughly $300 r_g$.

To achieve a MAD accretion disk, we initialize the magnetic

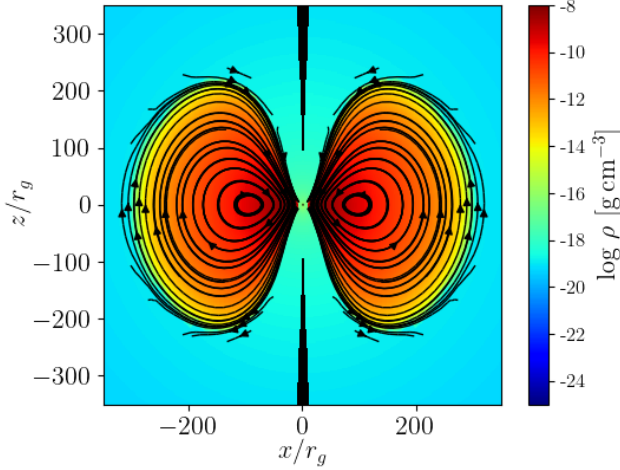


Figure B1. Here we show the gas density (colors) and magnetic field (streamlines) of the initial torus.

field as a large dipolar field by setting the vector potential scaled by the mass density

$$A_\varphi = \max\left(\rho r^3 \sin^3(\vartheta) \sin(r/\lambda), 0\right). \quad (\text{B7})$$

Here ρ is specifically the gas density of the torus, which is set to -1 outside of the initial torus so there is no magnetic field outside of it. The wavelength $\lambda = 9600 r_g$, which is much larger than the initial torus to ensure only one sign throughout. Starting from the vector potential guarantees that the magnetic field is divergence free. We set the magnetic field strength by scaling it relative to the gas pressure with $\beta_g = 10^{-3}$. This leads to the accumulation of magnetic field of only one polarization and the BH builds up a large magnetic flux quite rapidly.

We run the initial state for a spin $a_* = 0$ and $a_* = 0.9$ for a total of $15,000 t_g$. To save on resources, we run the first $10,000 t_g$ in 2D $r - \vartheta$ coordinates and then regrid to the full 3D grid. When we perform the regrid, a 5% perturbation is applied to the azimuthal velocity u^φ to break the symmetry. We find that $5000 t_g$ is enough for the system to become fully asymmetrical as in standard MADs. We show the gas density and field lines of the initial state in Figure B1. We show the simulation history for both BH spins prior to injecting the TDE stream in Figure B2.

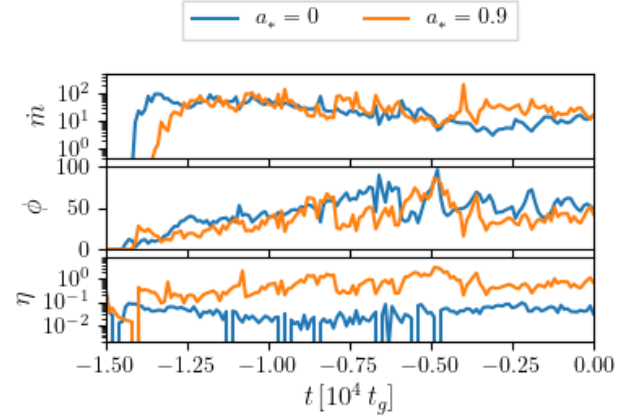


Figure B2. Here we show the initial evolution of each BH spin model prior to stream injection.